

Spinor Bose-Einstein Condensate Interferometer within the Undepleted Pump Approximation: Role of the Initial State

Jianwen Jie,^{1,*} Q. Guan,^{1,†} and D. Blume^{1,‡}

¹*Homer L. Dodge Department of Physics and Astronomy,
The University of Oklahoma, 440 W. Brooks Street, Norman, Oklahoma 73019, USA*

(Dated: 05/04/2019)

Most interferometers operate with photons or dilute, non-condensed cold atom clouds in which collisions are strongly suppressed. Spinor Bose-Einstein condensates (BECs) provide an alternative route toward realizing three-mode interferometers; in this realization, spin-changing collisions provide a resource that generates mode entanglement. Working in the regime where the pump mode, i.e., the $m = 0$ hyperfine state, has a much larger population than the side or probe modes ($m = \pm 1$ hyperfine states), $f = 1$ spinor BECs approximate SU(1,1) interferometers. We derive analytical expressions within the undepleted pump approximation for the phase sensitivity of such an SU(1,1) interferometer for two classes of initial states: pure Fock states and coherent spin states. The interferometer performance is analyzed for initial states without seeding, with single-sided seeding, and with double-sided seeding. The validity regime of the undepleted pump approximation is assessed by performing quantum calculations for the full spin Hamiltonian. Our analytical results and the associated dynamics are expected to guide experiments as well as numerical studies that explore regimes where the undepleted pump approximation makes quantitatively or qualitatively incorrect predictions.

I. INTRODUCTION

Quantum enhanced measurement protocols or quantum metrology refer to improving the precision measurement of a physical parameter or physical parameters using quantum protocols [1, 2]. Nowadays, quantum metrology is a powerful workhorse across physics, including areas as diverse as gravitational wave detection [3–5]; sensing applications [6] such as magnetometry [7, 8], gravitometry [9], and electric field determinations [10]; optical communication [11]; and image reconstruction [12, 13].

A classical approach for improving the estimation would repeat the measurement on N identical but independent systems or uncorrelated particles. For single parameter estimations, such an approach leads to a $1/\sqrt{N}$ scaling, which is typically referred to as standard quantum limit [4] or shot noise limit [14, 15]. Beyond (i.e., better than) the standard quantum limit performance can be achieved by taking advantage of quantum resources. Caves pointed out in 1981 [4] that squeezed states can improve the performance to a $1/N$ scaling. Motivated by the heuristic phase-particle number Heisenberg uncertainty relation $\Delta\theta\Delta N \geq 1$, Holland and Burnett [16] referred to the $1/N$ performance as “Heisenberg limit”. Unfortunately, unique definitions of the standard quantum limit and the Heisenberg limit are not available [2]. Quite generally, to specify these limits, the classical resources need to be defined and the improvement of the parameter estimation due to the additional quantum resources needs to be quantified.

Assuming a generic set-up that consists of three components—(i) input, (ii) “actual device”, and (iii) measurement and parameter estimation—one can attempt to improve the performance by optimizing either of the three components listed above. The present work focuses on quantifying the performance of a paradigmatic device, namely an interferometer, using established formulations for the parameter estimation: the phase sensitivities $\Delta\theta_{\text{QCR}}$ and $\Delta\theta_{\text{ep}}$ that are, respectively, derived from the quantum Cramer-Rao bound [17–19] and error propagation [1].

The interferometer considered is an SU(1,1) interferometer based on a $f = 1$ spinor Bose-Einstein condensate (BEC) [20, 21] with three internal hyperfine components, namely the hyperfine states with projection quantum numbers $m = +1$, $m = 0$, and $m = -1$ (f denotes the total spin angular momentum of the atom). An SU(1,1) interferometer can be constructed by replacing the passive beam splitters in a Mach-Zehnder interferometer by active non-linear parametric amplifiers, which can generate quantum correlations and entanglement [14].

Our study is motivated by the quest to get a handle on the role played by correlations and entanglement of the initial state and of the state during the amplification step. Given a device and parameter estimation scheme, how does the absolute performance depend on the initial state? Given a certain class of initial states, what are the device parameters that yield the best absolute phase sensitivity? Besides providing general insight and being important for studies in the regime where the undepleted pump approximation holds, our results are expected to provide guidance for spinor BEC based interferometer studies that operate outside the SU(1,1) regime.

Treating the spinor BEC in the single-mode approximation [22] and further working in the undepleted pump approximation [23], we report explicit analytic expres-

* Jianwen.Jie1990@gmail.com

† gqz0001@gmail.com

‡ doerte.blume-1@ou.edu

sions for the phase sensitivity and a number of auxiliary observables for two classes of initial states: pure Fock states and coherent spin states. We consider the situations where all atoms are in the $m = 0$ state and the side modes are empty (“vacuum state” [24]), the majority of atoms is in the $m = 0$ state and either the $m = +1$ mode or $m = -1$ mode has a small population (single-sided seeding), and the majority of atoms is in the $m = 0$ state and the $m = +1$ and $m = -1$ modes both have small populations (double-sided seeding). For selected observables, we present analytic expressions for an arbitrary pure initial state. Physical interpretations of the analytical expressions are presented. The validity regime of the undepleted pump approximation is assessed by simulating the entire interferometer sequence for the full spin Hamiltonian numerically.

The remainder of this paper is organized as follows. Sections II A and II B introduce the spin Hamiltonian that underlies this work and the basic operating principle of a spinor BEC based interferometer, respectively. The parameter estimation procedures considered in this work are introduced in Sec. II C and the undepleted pump approximation is introduced in Sec. II D. The equations of motion within this approximation and their solutions are introduced in Secs. III A and III B and explicit analytical results for the side mode population and the corresponding fluctuation are presented in Sec. III C. Section IV analyzes our analytical results. Two classes of initial states are considered: pure Fock states (see Sec. IV A) and coherent spin states (see Sec. IV B). Finally, Sec. V presents a conclusion.

II. PROBLEM DEFINITION AND THEORETICAL BACKGROUND

A. Full spin Hamiltonian

Our description accounts for the three hyperfine states of an $f = 1$ spinor BEC consisting of N atoms within the single-mode approximation, which assumes that the spatial degrees of freedom are integrated out [22, 25]. As a result, the dynamics is governed by the spin Hamiltonian \hat{H}_{spin} , which treats each atom as a structureless spin-1 “object” that undergoes two-body s -wave collisions [25],

$$\begin{aligned} \hat{H}_{\text{spin}}(c, q) = & \frac{c}{N} \left(\hat{a}_{+1}^\dagger \hat{a}_{-1}^\dagger \hat{a}_0 \hat{a}_0 + \text{h.c.} \right) \\ & + \frac{c}{N} \left(\hat{N}_0 - \frac{1}{2} \right) \left(\hat{N}_{+1} + \hat{N}_{-1} \right) \\ & + q \left(\hat{N}_{+1} + \hat{N}_{-1} \right). \end{aligned} \quad (1)$$

The first term on the right hand side of Eq. (1) describes spin-changing collisions, also referred to as spin-mixing dynamics; this term is identical to the four-wave mixing term in nonlinear quantum optics [14]. The second term on the right hand side of Eq. (1) corresponds to the collisional shift and the third term is a single-particle shift.

For reasons that will become clear in Sec. II B, we refer to this term of the Hamiltonian as linear phase shifter (LPS) Hamiltonian \hat{H}_{LPS} ,

$$\hat{H}_{\text{LPS}}(q) = q \left(\hat{N}_{+1} + \hat{N}_{-1} \right). \quad (2)$$

The operators \hat{a}_m^\dagger and \hat{a}_m satisfy the bosonic commutation relation $[\hat{a}_m, \hat{a}_m^\dagger] = 1$ (\hat{a}_m^\dagger creates and \hat{a}_m destroys an atom in hyperfine state $|f = 1, m\rangle$) and the atom number operator \hat{N}_m is defined through $\hat{N}_m = \hat{a}_m^\dagger \hat{a}_m$. The coefficient q contains a “Zeeman contribution” q_B from an external magnetic field and a contribution q_{MW} from a microwave field, $q = q_B + q_{\text{MW}}$ [26, 27]. The strength c ,

$$c = \bar{c} \bar{n}, \quad (3)$$

of the collision terms is determined by the mean spatial density \bar{n} and the coefficient \bar{c} , which is proportional to the difference between the scattering lengths a_F for two atoms with total spin angular momentum $F = 0$ and $F = 2$,

$$\bar{c} = \frac{2\pi\hbar^2}{\mu} \frac{a_2 - a_0}{3}. \quad (4)$$

Here, μ is the reduced two-body mass. In typical ^{23}Na and ^{87}Rb BEC experiments, $|c/h|$ is of the order of 20 Hz (\bar{c} and c are both positive for ^{23}Na and both negative for ^{87}Rb) and q/h can be tuned from negative values to zero to values much larger than $|c/h|$ [26, 27].

B. Spinor BEC interferometer

The three-mode spinor BEC interferometer takes an initial state $|\Psi(0)\rangle$, time evolves it under the spin Hamiltonian \hat{H}_{spin} , and then performs a measurement or measurements that form the basis for determining the phase sensitivity [see Fig. 1(a)]. In our work, $|\Psi(0)\rangle$ is a pure state; more generally, one could consider a mixed initial state $\hat{\rho}(0)$. The time evolution is, as shown in Fig. 1(b), divided into three time intervals of lengths t_1 , t_2 , and t_3 .

1. The first time sequence ($t = 0$ to $t = t_1$), which is referred to as “state preparation”, applies $\hat{H}_{\text{spin}}(c_1, q_1)$ to the initial state $|\Psi(0)\rangle$,

$$|\Psi(t_1)\rangle = e^{-i\hat{H}_{\text{spin}}(c_1, q_1)t_1/\hbar} |\Psi(0)\rangle. \quad (5)$$

2. The second, “phase encoding” time sequence ($t = t_1$ to $t = t_1 + t_2$) imprints the relative phase $\theta = 2q_{\text{ps}}t_2/\hbar$ by applying the linear phase shifter Hamiltonian $\hat{H}_{\text{LPS}}(q_{\text{ps}})$, which is characterized by the generator $(\hat{N}_{+1} + \hat{N}_{-1})/2$ [19],

$$|\Psi(t_1 + t_2)\rangle = e^{-i\hat{H}_{\text{LPS}}(q_{\text{ps}})t_2/\hbar} |\Psi(t_1)\rangle. \quad (6)$$

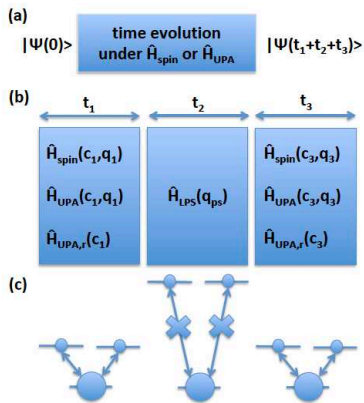


FIG. 1. (Color online) Schematic of interferometer. (a) Basic layout. The initial state $|\Psi(0)\rangle$ gets fed into the interferometer at time $t = 0$. At time $t = t_1 + t_2 + t_3$, measurements are made on $|\Psi(t_1 + t_2 + t_3)\rangle$. The present paper investigates how the phase sensitivity $\Delta\theta_{\text{ep}}$, obtained from $|\Psi(t_1 + t_2 + t_3)\rangle$, depends on the initial state $|\Psi(0)\rangle$ and how the phase sensitivity can be minimized for a given $|\Psi(0)\rangle$ by tweaking the parameters of the Hamiltonian that governs the time evolution. (b) Break-down of the three-step interferometer sequence. During step 1., the dynamics is governed by $\hat{H}_{\text{spin}}(c_1, q_1)$, $\hat{H}_{\text{UPA}}(c_1, q_1)$, or $\hat{H}_{\text{UPA},r}(c_1)$. During step 2., the dynamics is governed by the linear phase shifter Hamiltonian $\hat{H}_{\text{LPS}}(q_{\text{ps}})$. During step 3., the dynamics is governed by $\hat{H}_{\text{spin}}(c_3, q_3)$, $\hat{H}_{\text{UPA}}(c_3, q_3)$, or $\hat{H}_{\text{UPA},r}(c_3)$. (c) The horizontal lines represent, from left to right, the hyperfine states $m = +1$, $m = 0$, and $m = -1$. The population of the $m = 0$ mode is much larger than that of the $m = \pm 1$ side modes. Spin-changing collisions play an important role during steps 1. and 3. of the interferometer sequence but are turned off during step 2..

If an appropriate Fano-Feshbach resonance [28] exists, the linear phase shifter Hamiltonian can be realized by tuning c to zero. In the absence of Fano-Feshbach resonances, the linear phase shifter Hamiltonian can be realized approximately by operating in the regime where $|q| \gg |c|$.

3. The third time sequence ($t = t_1 + t_2$ to $t = t_1 + t_2 + t_3$), which is referred to as “read out”, applies the spin-mixing Hamiltonian $\hat{H}_{\text{spin}}(c_3, q_3)$,

$$|\Psi(t_1 + t_2 + t_3)\rangle = e^{-i\hat{H}_{\text{spin}}(c_3, q_3)t_3/\hbar}|\Psi(t_1 + t_2)\rangle. \quad (7)$$

The mean number $N_s(t)$ of atoms in the $m = +1$ and -1 side modes and the corresponding quantum fluctuation $\Delta N_s(t)$ play an important role in analyzing the interferometer performance, which is quantified by the phase sensitivity (see Sec. II C for details). We define

$$\hat{N}_s = \hat{N}_{+1} + \hat{N}_{-1}, \quad (8)$$

$$N_s(t) = \langle \hat{N}_s \rangle = \langle \Psi(t) | \hat{N}_s | \Psi(t) \rangle, \quad (9)$$

and

$$\Delta N_s(t) = \sqrt{\langle (\hat{N}_s)^2 \rangle - \langle \hat{N}_s \rangle^2}. \quad (10)$$

The quantities $N_m(t)$ and their quantum fluctuations are defined analogously.

C. Quantifying the interferometer performance

To quantify the interferometer performance, we consider two different quantities, namely $\Delta\theta_{\text{ep}}$ and $\Delta\theta_{\text{QCR}}$. We emphasize that the discussion in this section is specific to the situation where the phase imprinting is based on the linear phase shifter Hamiltonian. Non-linear phase imprinting protocols modify how the various limits scale with the number of (active) atoms [19, 29, 30].

The phase sensitivity $\Delta\theta_{\text{ep}}$ is obtained through error propagation,

$$\Delta\theta_{\text{ep}} = \frac{\Delta N_s(t_1 + t_2 + t_3)}{|\partial_\theta N_s(t_1 + t_2 + t_3)|}. \quad (11)$$

Since it is evaluated at $t = t_1 + t_2 + t_3$, it depends on all three steps of the interferometer sequence as well as the initial state. The fact that $\Delta\theta_{\text{ep}}$ is fully determined by the characteristics of the side mode population makes it readily accessible to cold atom experiments.

A stringent limit on the parameter estimation is set by the phase sensitivity $\Delta\theta_{\text{QCR}}$, which is derived from the quantum Cramer-Rao bound [1, 17],

$$\Delta\theta_{\text{QCR}}[|\Psi(t_1)\rangle, \hat{N}_s/2] = \frac{1}{\sqrt{F_Q[|\Psi(t_1)\rangle, \hat{N}_s/2]}}. \quad (12)$$

Here, F_Q denotes the quantum Fischer information. For the interferometer with linear phase shifter, the quantum Fischer information depends on $|\Psi(t_1)\rangle$ and the generator $\hat{N}_s/2$ that is associated with the linear phase shifter Hamiltonian. Importantly, the phase sensitivity $\Delta\theta_{\text{QCR}}$ is independent of the readout step. In general, one finds

$$\Delta\theta_{\text{ep}} \geq \Delta\theta_{\text{QCR}}[|\Psi(t_1)\rangle, \hat{N}_s/2], \quad (13)$$

i.e., the quantum Cramer-Rao bound provides a lower bound for the error propagation based sensitivity estimator. For pure states $|\Psi(t_1)\rangle$ and linear phase imprinting generated by $\hat{N}_s/2$, one finds [1]

$$\Delta\theta_{\text{QCR}}[|\Psi(t_1)\rangle, \hat{N}_s/2] = \frac{1}{\Delta N_s(t_1)}. \quad (14)$$

Ideally, one would like to operate in the regime where the quantity $\Delta\theta_{\text{ep}}/\Delta\theta_{\text{QCR}}$ is close to one, i.e., in the regime where the error propagation based sensitivity $\Delta\theta_{\text{ep}}$ is as close as possible to the best achievable phase sensitivity.

For comparison, we also report the Heisenberg limit $\Delta\theta_{\text{HL}}$, which we take to be defined in terms of the number $N_s(t_1)$ of atoms in the side modes at time t_1 ,

$$\Delta\theta_{\text{HL}} = \frac{1}{N_s(t_1)}; \quad (15)$$

$N_s(t_1)$ can be thought of as the number of “active atoms” during the phase imprinting stage of the SU(1,1) interferometer. In this context, it is worthwhile mentioning that there exist a variety of definitions and interpretations of the Heisenberg limit [1, 17–19, 24, 29–32]. Section IV shows that the SU(1,1) interferometer with linear phase imprinting allows for situations where the quantum Cramer-Rao bound based phase sensitivity, which provides a strict lower bound, is larger than the Heisenberg limit defined in Eq. (15), thereby underpinning the notion that the Heisenberg limit, as defined in Eq. (15), should not be interpreted as defining the ultimate or best achievable performance.

D. Undepleted pump approximation

The interferometer sequence introduced in Sec. II B has, in general, to be modeled numerically. Analytical results can, however, be obtained within the undepleted pump approximation (UPA) [23, 24, 33], which replaces the operators \hat{a}_0^\dagger and \hat{a}_0 by the square-root of the mean number \bar{N}_0 of particles in the $m = 0$ mode at time $t = 0$,

$$\bar{N}_m = \langle \Psi(0) | \hat{N}_m | \Psi(0) \rangle. \quad (16)$$

The approximation is consistent with considering a large reservoir of atoms in the $m = 0$ pump mode. Physically, the undepleted pump approximation assumes that the majority of atoms occupies the $m = 0$ pump mode. This places restrictions on the initial state and on the operating time $t_1 + t_2 + t_3$ of the interferometer, since only a small fraction of the atoms should get pumped (i.e., scattered) into the $m = +1$ and $m = -1$ side modes during the time evolution.

Dropping the constant energy shift $-c(\bar{N}_0 - 1/2)/N - q$, the spin Hamiltonian \hat{H}_{spin} in the undepleted pump approximation reads

$$\begin{aligned} \hat{H}_{\text{UPA}}(c, q) = & \frac{2\bar{N}_0 c}{N} \hat{K}_x \\ & + 2 \left[\frac{\bar{N}_0 c}{N} \left(1 - \frac{1}{2\bar{N}_0} \right) + q \right] \hat{K}_z, \end{aligned} \quad (17)$$

where the operators \hat{K}_x , \hat{K}_y , and \hat{K}_z are elements of the SU(1,1) group [14],

$$\hat{K}_x = \frac{1}{2} \left(\hat{a}_{+1}^\dagger \hat{a}_{-1}^\dagger + \hat{a}_{+1} \hat{a}_{-1} \right), \quad (18)$$

$$\hat{K}_y = \frac{1}{2i} \left(\hat{a}_{+1}^\dagger \hat{a}_{-1}^\dagger - \hat{a}_{+1} \hat{a}_{-1} \right), \quad (19)$$

and

$$\hat{K}_z = \frac{1}{2} \left(\hat{N}_s + 1 \right). \quad (20)$$

Since the Hamiltonian \hat{H}_{UPA} can be written in terms of the elements of the SU(1,1) group, the resulting interferometer is an SU(1,1) interferometer. It is important to

realize that \hat{H}_{UPA} does not conserve the particle number. In the context of photons, this is very natural. In the context of spinor BECs as considered in this paper, this is not natural since the number of atoms is, neglecting one-, two-, and higher-body losses, conserved. We elaborate on this discussion in Sec. IV B and Appendix C.

Looking ahead, we also define the simpler “resonant” Hamiltonian $\hat{H}_{\text{UPA,r}}$, which assumes that the collisional and Zeeman shifts cancel each other, as a special case. Setting q in \hat{H}_{UPA} to q_c ,

$$q_c = -\frac{\bar{N}_0 c}{N} \left(1 - \frac{1}{2\bar{N}_0} \right), \quad (21)$$

we obtain

$$\hat{H}_{\text{UPA,r}}(c) = \frac{2\bar{N}_0 c}{N} \hat{K}_x. \quad (22)$$

Since \bar{N}_0 is assumed to be close to N and N is much greater than 1, we have $q_c \simeq -c$.

Our analytical results presented in Secs. III and IV are obtained for the standard three-step sequence of the SU(1,1) interferometer, which is identical to the sequence introduced in the previous section with \hat{H}_{spin} replaced by \hat{H}_{UPA} .

III. SOLUTIONS FOR SU(1,1) INTERFEROMETER

A. Equations of motion

To simulate the SU(1,1) interferometer sequence discussed in the previous section, we work in the Heisenberg picture. The equations of motion for the time-dependent operators \hat{a}_{+1} and \hat{a}_{-1} then read [14]

$$i\hbar \partial_t \hat{a}_{\pm 1}(t) = [\hat{a}_{\pm 1}(t), \hat{H}_{\text{UPA}}(t)]. \quad (23)$$

Solving the coupled linear equations implied by Eq. (23), one obtains [14]

$$\begin{pmatrix} \hat{a}_{+1}(t_1 + t_2 + t_3) \\ \hat{a}_{-1}^\dagger(t_1 + t_2 + t_3) \end{pmatrix} = \begin{pmatrix} \tilde{A} & \tilde{B} \\ \tilde{B}^* & \tilde{A}^* \end{pmatrix} \begin{pmatrix} \hat{a}_{+1}(0) \\ \hat{a}_{-1}^\dagger(0) \end{pmatrix}, \quad (24)$$

where the “transfer matrix” is constructed by applying three consecutive operations (one for each of the three interferometer steps),

$$\begin{pmatrix} \tilde{A} & \tilde{B} \\ \tilde{B}^* & \tilde{A}^* \end{pmatrix} = \begin{pmatrix} A_3 & B_3 \\ B_3^* & A_3^* \end{pmatrix} \begin{pmatrix} e^{-i\theta/2} & 0 \\ 0 & e^{i\theta/2} \end{pmatrix} \begin{pmatrix} A_1 & B_1 \\ B_1^* & A_1^* \end{pmatrix}. \quad (25)$$

Performing the matrix multiplication, one finds

$$\tilde{A} = A_1 A_3 e^{-i\theta/2} + B_1^* B_3 e^{i\theta/2} \quad (26)$$

and

$$\tilde{B} = B_1 A_3 e^{-i\theta/2} + A_1^* B_3 e^{i\theta/2}. \quad (27)$$

Note that \tilde{A} and \tilde{B} depend on t_1 , θ , and t_3 (recall that θ depends on t_2); for notational simplicity, these dependencies are not explicitly indicated. The quantities A_j and B_j depend on t_j . The next section reports explicit expressions for A_j , B_j , $|\tilde{A}|^2$, and $|\tilde{B}|^2$ that are applicable to arbitrary parameter combinations.

B. General solution

Even though steps 1. and 3. of the interferometer sequence depend on six independent, experimentally controllable parameters (namely c_1 , c_3 , q_1 , q_3 , t_1 , and t_3), the solutions for A_j and B_j ($j = 1$ and 3) within the undepleted pump approximation can be expressed in terms of four dimensionless parameters ξ_1 , ξ_3 , χ_1 , and χ_3 , which are defined through

$$\xi_j = \frac{\bar{N}_0 c_j t_j}{N \hbar} \quad (28)$$

and

$$\chi_j = \sqrt{1 - \left(1 - \frac{q_j}{q_{c,j}}\right)^2 \left(1 - \frac{1}{2\bar{N}_0}\right)^2}. \quad (29)$$

Here, $q_{c,j}$ is given by Eq. (21) with c replaced by c_j . In what follows, we refer to ξ_1 , ξ_3 , χ_1 , and χ_3 as interferometer parameters. As an example, Figs. 2(a) and 2(b) show the dependence of ξ_j on the time t_j and the dependence of the real and imaginary parts of χ_j on the dimensionless parameter $q_j/q_{c,j}$ for a ^{23}Na condensate with $\bar{N}_0 = N = 10000$ (see Appendix A for details).

Using the parameters defined in Eqs. (28) and (29), A_j and B_j can be written as

$$A_j = \cosh(\xi_j \chi_j) - \frac{i\sqrt{1 - \chi_j^2}}{\chi_j} \sinh(\xi_j \chi_j) \quad (30)$$

and

$$B_j = -\frac{i}{\chi_j} \sinh(\xi_j \chi_j). \quad (31)$$

Note that the interferometer performance may depend on additional parameters that characterize the initial state such as the initial seeding fraction; A_j and B_j are, however, independent of these additional parameters. One finds

$$|\tilde{A}|^2 = (|A_1 A_3| - |B_1 B_3|)^2 + 2|A_1 A_3 B_1 B_3| \times [1 + \cos(\theta - \gamma_{A_1} - \gamma_{A_3} - \gamma_{B_1} + \gamma_{B_3})] \quad (32)$$

and

$$|\tilde{B}|^2 = (|A_1 B_3| - |A_3 B_1|)^2 + 2|A_1 A_3 B_1 B_3| \times [1 + \cos(\theta - \gamma_{A_1} - \gamma_{A_3} - \gamma_{B_1} + \gamma_{B_3})], \quad (33)$$

where the phases γ_{A_j} and γ_{B_j} are given by $\gamma_{A_j} = \arg(A_j)$ and $\gamma_{B_j} = \arg(B_j)$, respectively. It can be checked that both $|A_j|^2 - |B_j|^2$ and $|\tilde{A}|^2 - |\tilde{B}|^2$ are equal to 1. Appendix B summarizes selected properties implied by Eqs. (28)-(31).

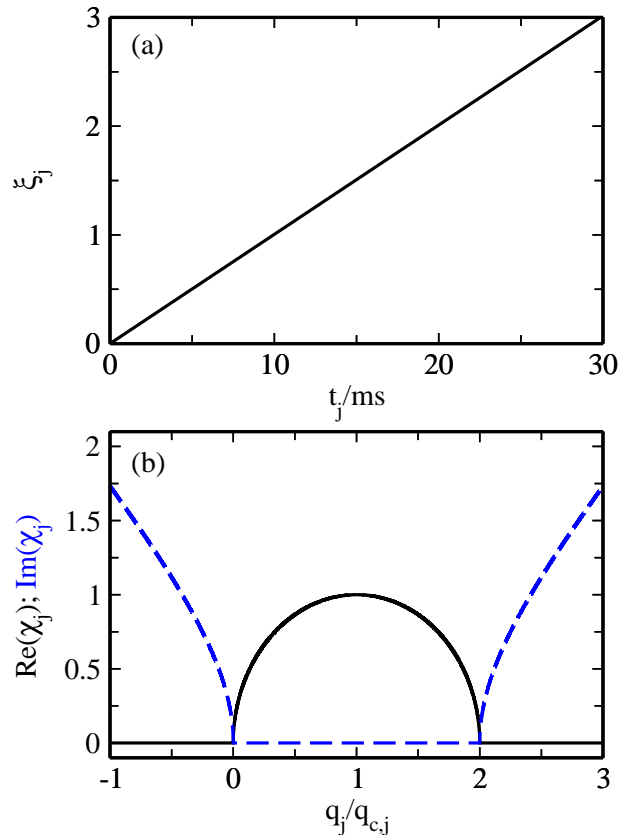


FIG. 2. (Color online) Dimensionless parameters ξ_j and χ_j that govern steps 1. and 3. of the interferometer sequence. (a) The solid line shows ξ_j as a function of t_j . (b) The solid and dashed lines show the real and imaginary parts of χ_j as a function of the dimensionless parameter $q_j/q_{c,j}$. The plots are made assuming a ^{23}Na condensate with $N = \bar{N}_0 = 10000$, $c_j/\hbar = 15.9956$ Hz, and $q_{c,j}/\hbar = -15.9948$ Hz (see Appendix A for details).

C. Side mode population and associated quantum fluctuation

Armed with explicit expressions for $\hat{a}_{+1}(t)$, $\hat{a}_{-1}^\dagger(t)$, $\hat{a}_{-1}(t)$, and $\hat{a}_{+1}^\dagger(t)$ for all t between 0 and $t_1 + t_2 + t_3$, the expectation value of the operator \tilde{N}_s and the corresponding quantum fluctuation at any time t can be calculated for any initial state $|\Psi(0)\rangle$, assuming the undepleted pump approximation is valid. We find

$$N_s(t_1 + t_2 + t_3) = |\tilde{A}|^2 + |\tilde{B}|^2 - 1 + \left(|\tilde{A}|^2 + |\tilde{B}|^2 \right) \overline{N}_s + 2 \left(\tilde{A}\tilde{B}^* \overline{P} + \text{c.c.} \right) \quad (34)$$

and

$$\Delta N_s(t_1 + t_2 + t_3) = 2|\tilde{A}\tilde{B}| \times \sqrt{1 + \overline{N}_s + 2\text{Cov}(\hat{P}^\dagger, \hat{P}) + \left[e^{2i(\gamma_{\tilde{A}} - \gamma_{\tilde{B}})} (\overline{\Delta P})^2 + \text{c.c.} \right]} + 2 \left[e^{i(\gamma_{\tilde{A}} - \gamma_{\tilde{B}})} \left(\overline{P} + \text{Cov}(\hat{N}_s, \hat{P}) \right) + \text{c.c.} \right] \mathcal{I} + (\overline{\Delta N}_s)^2 \mathcal{I}^2, \quad (35)$$

where $\gamma_{\tilde{A}} = \arg(\tilde{A})$ and $\gamma_{\tilde{B}} = \arg(\tilde{B})$. The quantity \mathcal{I} is independent of the properties of the initial state,

$$\mathcal{I} = \frac{|\tilde{A}|^2 + |\tilde{B}|^2}{2|\tilde{A}\tilde{B}|}. \quad (36)$$

In Eqs. (34) and (35), \overline{N}_s is the number of atoms in the side modes at time zero and \overline{P} ,

$$\overline{P} = \langle \Psi(0) | \hat{P} | \Psi(0) \rangle, \quad (37)$$

is defined in terms of the “pair annihilation operator”,

$$\hat{P} = \hat{a}_{+1} \hat{a}_{-1}. \quad (38)$$

The quantities $\overline{\Delta N}_s$ and $\overline{\Delta P}$ denote the quantum fluctuations associated with \overline{N}_s and \overline{P} , respectively,

$$\overline{\Delta O} = \Delta O(0) \quad (39)$$

(here, O denotes an arbitrary observable). Last, the quantity $\text{Cov}(\hat{O}_1, \hat{O}_2)$ denotes the covariance of the operators \hat{O}_1 and \hat{O}_2 at time zero,

$$\overline{\text{Cov}(\hat{O}_1, \hat{O}_2)} = \langle \Psi(0) | \hat{O}_1 \hat{O}_2 | \Psi(0) \rangle - \langle \Psi(0) | \hat{O}_1 | \Psi(0) \rangle \langle \Psi(0) | \hat{O}_2 | \Psi(0) \rangle. \quad (40)$$

As written, Eqs. (34) and (35) apply to an arbitrary pure initial state $|\Psi(0)\rangle$. These equations also apply to an initial mixed state $\hat{\rho}(0)$, provided \overline{O} , $\overline{\Delta O}$, and $\overline{\text{Cov}(\hat{O}_1, \hat{O}_2)}$ are generalized. For example, \overline{O} would be defined as $\text{Tr}[\hat{\rho}(0)\hat{O}]$ and analogous generalizations would apply for the other expectation values.

As already discussed earlier, $|\partial_\theta N_s(t_1 + t_2 + t_3)|$ and $\Delta N_s(t_1 + t_2 + t_3)$ govern the phase sensitivity $\Delta\theta_{\text{ep}}$. It follows from Eqs. (34) and (35) that the interferometer performance depends on two aspects: (i) the initial state through the quantities \overline{N}_s , $\overline{\Delta N}_s$, \overline{P} , $\overline{\Delta P}$, $\overline{\text{Cov}(\hat{N}_s, \hat{P})}$, and $\overline{\text{Cov}(\hat{P}^\dagger, \hat{P})}$; and (ii) the interferometer device through \tilde{A} and \tilde{B} . Recall, \tilde{A} and \tilde{B} are, within the undepleted pump approximation, fully determined by the five dimensionless parameters ξ_1 , ξ_3 , χ_1 , χ_3 , and θ . Importantly, the first term on the right hand side of Eq. (34) and the first term inside the square root sign of

Eq. (35) depend only on the interferometer device while all other terms “mix” the interferometer device and the initial state.

We can also look at the quantum Cramer-Rao bound $1/\Delta N_s(t_1)$. Equations (34) and (35) yield $N_s(t_1)$ and $\Delta N_s(t_1)$ if \tilde{A} , \tilde{B} , $\gamma_{\tilde{A}}$, and $\gamma_{\tilde{B}}$ are replaced by A_1 , B_1 , γ_{A_1} , and γ_{B_1} , respectively. It follows that $N_s(t_1)$ depends, within the undepleted pump approximation, on the initial state only through \overline{N}_s and \overline{P} , i.e., the initial seeding and the initial “pair correlation”. If \overline{N}_s and \overline{P} are zero, $N_s(t_1)$ grows exponentially with increasing $|\xi_1 \chi_1|$ if χ_1 is real. Maximal growth is obtained for $q_1 = q_{c,1}$ (corresponding to $\chi_1 = 1$), with a growth rate of $\overline{N}_0 c_1 / (N\hbar)$. The regime where $N_s(t_1)$ grows exponentially is referred to as dynamical instability [34]. Since the fluctuation $\Delta N_s(t_1)$ depends on the initial state, the quantum Cramer-Rao bound as well as $\Delta\theta_{\text{ep}}$ can be controlled, at least partially, by adjusting the initial state.

D. Special cases

The solutions presented in Secs. III B and III C simplify significantly for the resonant case, i.e., when q_j is set to $q_{c,j}$ and \hat{H}_{UPA} reduces to $\hat{H}_{\text{UPA},\text{r}}$. Columns 1 and 2 of Table I summarize selected expressions for two resonant cases ($\chi_1 = \chi_3 = 1$), namely the resonant symmetric interferometer for which $\xi = \xi_1 = \xi_3$ and the resonant asymmetric interferometer for which $\xi_1 \neq \xi_3$. In the former case, the interferometer is fully characterized by the dimensionless parameter ξ and the phase θ ; this case has been considered in Ref. [24] for the vacuum state. In the latter case, the interferometer is fully characterized by the two dimensionless parameters ξ_1 and ξ_3 and the phase θ ; this case has been considered in Ref. [23] for a class of density matrices.

The solutions also simplify notably for the non-resonant symmetric interferometer for which $\xi = \xi_1 = \xi_3 \neq 1$ and $\chi = \chi_1 = \chi_3$. In this case, the interferometer is fully characterized by the two dimensionless parameters ξ and χ as well as the phase θ . This case has been considered in Ref. [35] and selected expressions are summarized in column 3 of Table I.

The SU(1,1) interferometer has a “time reversal sym-

metry” when $N_s(t)$ and $\Delta N_s(t)$ return at $t = t_1 + t_2 + t_3$

TABLE I. Summary of the solutions within the undepleted pump approximation to the equations of motion for three special cases: resonant symmetric interferometer, resonant asymmetric interferometer, and non-resonant symmetric interferometer.

resonant symmetric $\xi_1 = \xi_3 = \xi; \chi_1 = \chi_3 = 1$	resonant asymmetric any $\xi_j; \chi_1 = \chi_3 = 1$	non-resonant symmetric $\xi_1 = \xi_3 = \xi; \chi_1 = \chi_3 = \chi$
$A_j = A = \cosh \xi$	$A_j = \cosh \xi_j$	$A_j = A = \cosh(\xi\chi) - \frac{\sqrt{1-\chi^2}}{\chi} \sinh(\xi\chi)$
$B_j = B = -i \sinh \xi$	$B_j = -i \sinh \xi_j$	$B_j = B = -i \sinh(\xi\chi)$
$\gamma_{A_j} = \gamma_A = 0$	$\gamma_{A_j} = \gamma_A = 0$	$\gamma_{A_j} = \gamma_A$
$\gamma_{B_j} = \gamma_B = -\text{sign}(\xi)\pi/2$	$\gamma_{B_j} = -\text{sign}(\xi_j)\pi/2$	$\gamma_{B_j} = \gamma_B$
$ \tilde{B} ^2 = \sinh^2(2\xi) \cos^2(\theta/2)$	$ \tilde{B} ^2 = \cosh^2 \xi_1 \sinh^2 \xi_3 + \cosh^2 \xi_3 \sinh^2 \xi_1 + 2 \cosh \xi_1 \cosh \xi_3 \sinh \xi_1 \sinh \xi_3 \cos(\theta - \gamma_{B_1} + \gamma_{B_3})$	$ \tilde{B} ^2 = 2 AB ^2 [1 + \cos(\theta - 2\gamma_A)]$

to their initial values \overline{N}_s and $\overline{\Delta N}_s$. For the symmetric interferometer (i.e., $\gamma_{A_1} = \gamma_{A_3} = \gamma_A$ and $\gamma_{B_1} = \gamma_{B_3} = \gamma_B$), \tilde{B} goes to zero at $t = t_1 + t_2 + t_3$ for $\theta = \pi + 2\gamma_A$. For this phase, we have (the time dependence of \tilde{A} is indicated explicitly for clarity)

$$N_s(t_1 + t_2 + t_3)|_{\theta=\pi+2\gamma_A} = |\tilde{A}(t_1 + t_2 + t_3)|^2 \overline{N}_s \quad (41)$$

and

$$\Delta N_s(t_1 + t_2 + t_3)|_{\theta=\pi+2\gamma_A} = |\tilde{A}(t_1 + t_2 + t_3)|^2 \overline{\Delta N}_s. \quad (42)$$

Thus, the symmetric SU(1,1) interferometer with $\theta = \pi + 2\gamma_A$ has a time reversal symmetry if the initial state has no seeding, i.e., if \overline{N}_s and $\overline{\Delta N}_s$ are equal to 0. If the interferometer is not only symmetric but also resonant (in this case, $\gamma_A = 0$) and if we consider $\theta = \pi$, then $\tilde{A}(t_1 + t_2 + t_3)$ goes to 1. Thus, the interferometer has time reversal symmetry even when the initial state has

non-zero seeding. An SU(1,1) interferometer that utilizes time reversal symmetry was realized experimentally in a spinor ^{87}Rb BEC [24].

IV. EXPLICIT RESULTS FOR VARIOUS INITIAL STATES

This section considers two typical classes of initial states $|\Psi(0)\rangle$: pure Fock states are discussed in Sec. IV A and coherent spin states in Sec. IV B. Selected properties of these two initial states are summarized in Table II. Even though our analytical results within the undepleted pump approximation are derived in the Heisenberg picture, this section takes the view point that the initial state is propagated in time and that the operators are time independent.

TABLE II. Properties of the initial states $|\Psi(0)\rangle$ considered in Sec. IV: vacuum state (VS), pure Fock state with single- and double-sided seeding (PFS,S and PFS,D), and coherent spin state with single- and double-sided seeding (CSS,S and CSS,D). The results are obtained within the undepleted pump approximation.

$ \Psi(0)\rangle$	\overline{N}_s	$\overline{\Delta N}_s$	\overline{P}	$\overline{\Delta P}$	$\overline{\text{Cov}(\hat{N}_s, \hat{P})}$	$\overline{\text{Cov}(\hat{P}^\dagger, \hat{P})}$
VS	0	0	0	0	0	0
PFS,S	\overline{N}_s	0	0	0	0	0
PFS,D	\overline{N}_s	0	0	0	0	$\overline{N}_+ \overline{N}_-$
CSS,S	\overline{N}_s	$\sqrt{\overline{N}_s}$	0	0	0	0
CSS,D	\overline{N}_s	$\sqrt{\overline{N}_s}$	$(\overline{N}_{+1} \overline{N}_{-1})^{1/2} \exp(-i\theta)$	0	0	0

A. Pure Fock state

Let the initial state be a pure Fock state (PFS) with \overline{N}_m atoms in mode m ,

$$|\Psi(0)\rangle = |\overline{N}_{+1}, \overline{N}_0, \overline{N}_{-1}\rangle.$$

This initial state describes a system with \overline{N} atoms, where $\overline{N} = \overline{N}_{-1} + \overline{N}_0 + \overline{N}_{+1}$. We refer to $|0, \overline{N}_0, 0\rangle$ as “vacuum state” (VS) [24]. The naming originates from the fact that the side modes, sometimes also referred to as probe modes, are initially empty. The vacuum state can be interpreted as a special case of a pure Fock state or a

special case of a coherent spin state (see Sec. IV B). The spin mixing dynamics during step 1. of the interferometer sequence can evolve the vacuum state to a state with significant entanglement [24]. If one or both of the side modes contain non-zero occupation at time $t = 0$, we refer to the initial state as seeded Fock state. Single-sided seeding is realized if \overline{N}_{+1} or \overline{N}_{-1} is non-zero and double-sided seeding if \overline{N}_{+1} and \overline{N}_{-1} are non-zero. We refer to the resulting states as pure Fock state with single-sided seeding (“PFS,S”) and double-sided seeding (“PFS,D”), respectively.

To calculate the phase sensitivity $\Delta\theta_{\text{ep}}$, we need to

determine the expectation value of \hat{N}_s and its quantum fluctuation at time $t_1 + t_2 + t_3$. Using the results for the pure Fock state with double-sided seeding from Table II, we find

$$N_s(t_1 + t_2 + t_3) = |\tilde{A}|^2 + |\tilde{B}|^2 - 1 + \left(|\tilde{A}|^2 + |\tilde{B}|^2\right) \bar{N}_s \quad (43)$$

and

$$\Delta N_s(t_1 + t_2 + t_3) = 2|\tilde{A}\tilde{B}|\sqrt{1 + \bar{N}_s + 2\bar{N}_{+1}\bar{N}_{-1}}. \quad (44)$$

Equations (43) and (44) show that initial seeding leads to an enhancement of the number of atoms in the side modes at the end of the interferometer sequence (i.e., speeds up the dynamics) and also enhances the quantum fluctuations. Physically, this can be interpreted as being due to Bose enhancement as a consequence of the non-zero initial seeding \bar{N}_s . The quantum fluctuation $\Delta N_s(t_1 + t_2 + t_3)$ does not only depend on \bar{N}_s but, for double-sided seeding, also on the actual distribution of the atoms among the two side modes, i.e., the value of $\bar{N}_{+1}\bar{N}_{-1}$. As shown in Eq. (47), a non-zero $\bar{N}_{+1}\bar{N}_{-1}$ leads to a degradation of the phase sensitivity of the SU(1,1) interferometer.

As an example, Fig. 3 compares our analytical results obtained within the undepleted pump approximation (solid lines) with the results obtained by evolving the initial state under the full spin Hamiltonian \hat{H}_{spin} , Eq. (1), through exact diagonalization (dashed lines) for a ^{23}Na condensate with $\bar{N}_0 = 10000$. It can be seen that the undepleted pump approximation captures the time dependence of N_s [see Fig. 3(a)] and ΔN_s [see Fig. 3(b)] well for $\xi_1 \lesssim 4$ (for the parameters employed, this corresponds to $t_1 \lesssim 40$ ms). For $\xi_1 \gtrsim 4$, the undepleted pump approximation results deviate not only quantitatively but, rather quickly, also qualitatively from the exact numerical results. From a practical point of view, 40 ms are sufficient for an interferometer experiment. For an initial state with $\bar{N}_s \neq 0$, the validity regime of the undepleted pump approximation tends to be somewhat more restricted.

From Eq. (43) one obtains

$$\partial_\theta N_s(t_1 + t_2 + t_3) = -4|A_1 A_3 B_1 B_3|(1 + \bar{N}_s) \times \sin(\theta - \gamma_{A_1} - \gamma_{A_3} - \gamma_{B_1} + \gamma_{B_3}). \quad (45)$$

Combining Eqs. (44) and (45), the phase sensitivity [see Eq. (11)] for the pure Fock state takes the form

$$\Delta\theta_{\text{ep,PFS}} = \Delta\theta_{\text{ep,VS}} f_{\text{PFS}}, \quad (46)$$

where f_{PFS} and $\Delta\theta_{\text{ep,VS}}$ are defined through

$$f_{\text{PFS}} = \frac{\sqrt{1 + \bar{N}_s + 2\bar{N}_{+1}\bar{N}_{-1}}}{1 + \bar{N}_s} \quad (47)$$

and

$$\Delta\theta_{\text{ep,VS}} = \frac{|\tilde{A}\tilde{B}|}{2|A_1 A_3 B_1 B_3 \sin(\theta - \gamma_{A_1} - \gamma_{A_3} - \gamma_{B_1} + \gamma_{B_3})|}, \quad (48)$$

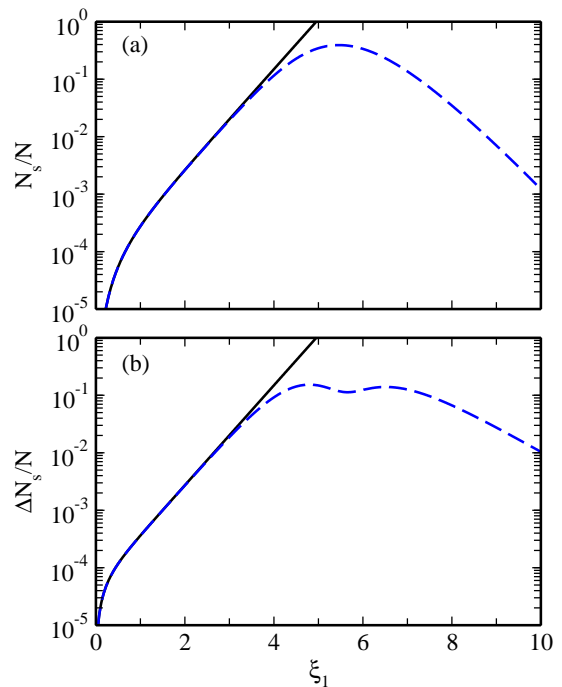


FIG. 3. (Color online) Benchmarking the undepleted pump approximation for the initial vacuum state $|0, \bar{N}_0, 0\rangle$. The solid lines show the undepleted pump approximation results for (a) N_s [Eq. (43)] and (b) ΔN_s [Eq. (44)] as a function of ξ_1 for $\chi_1 = 1$. For comparison, the dashed lines show our exact numerical results for the full spin Hamiltonian $\hat{H}_{\text{spin}}(c_1, q_1)$ with $N = \bar{N}_0 = 10000$, $c_1/h = 15.9956$ Hz and $q_1/h = -15.9948$ Hz (these are the same parameters as used in Fig. 2). The agreement is good for $\xi_1 \lesssim 4$.

respectively. The quantity $\Delta\theta_{\text{ep,VS}}$ depends on θ through the sin term in the denominator and through the cos terms in $|\tilde{A}\tilde{B}|$,

$$|\tilde{A}\tilde{B}| = \sqrt{s + t [1 + \cos(\theta - \gamma_{A_1} - \gamma_{A_3} - \gamma_{B_1} + \gamma_{B_3})] + \frac{u}{2} [1 + \cos(\theta - \gamma_{A_1} - \gamma_{A_3} - \gamma_{B_1} + \gamma_{B_3})]^2}, \quad (49)$$

where

$$s = (|A_1 A_3| - |B_1 B_3|)^2 + (|B_1 A_3| - |A_1 B_3|)^2, \quad (50)$$

$$t = 2|A_1 A_3 B_1 B_3| \times \left[(|A_1 A_3| - |B_1 B_3|)^2 + (|B_1 A_3| - |A_1 B_3|)^2 \right], \quad (51)$$

and

$$u = 8|A_1 A_3 B_1 B_3|^2. \quad (52)$$

Since f_{PFS} reduces to 1 for the vacuum state $|0, \bar{N}_0, 0\rangle$, the phase sensitivity for the vacuum state is given by $\Delta\theta_{\text{ep,VS}}$. In this case, $\Delta\theta_{\text{ep,VS}}$ can be interpreted as a phase sensitivity; for other initial pure Fock states, in contrast, $\Delta\theta_{\text{ep,VS}}$ is not by itself a phase sensitivity but a function that, together with f_{PFS} , determines the phase sensitivity $\Delta\theta_{\text{ep,PFS}}$. Since $\Delta\theta_{\text{ep,VS}}$ is determined by the ‘‘actual device’’ or interferometer parameters (i.e., it is independent of the initial state) and f_{PFS} is determined by the initial state (i.e., it is independent of the interferometer parameters), the minimum of $\Delta\theta_{\text{ep,PFS}}$ is determined by independently minimizing $\Delta\theta_{\text{ep,VS}}$ and f_{PFS} . In what follows, we first analyze f_{PFS} and then $\Delta\theta_{\text{ep,VS}}$.

Since f_{PFS} reduces to 1 in the absence of initial seeding, i.e., for $\bar{N}_s = 0$, we refer to it as ‘‘seeding factor’’. We find

$$\sqrt{\frac{1}{\bar{N}_s + 1}} \leq f_{\text{PFS}} \leq \sqrt{\frac{1}{2} \left[1 + \frac{1}{(\bar{N}_s + 1)^2} \right]} \leq 1. \quad (53)$$

For non-zero \bar{N}_s , f_{PFS} is always smaller than one. Equations (47) and (53), which apply to arbitrary initial pure Fock states (assuming the undepleted pump approximation is applicable), show:

- Initial seeding decreases the absolute phase sensitivity and hence improves the absolute interferometer performance.
- For a fixed finite \bar{N}_s and fixed interferometer parameters, initial single-sided seeding leads to the best interferometer performance (smallest f_{PFS}) and initial balanced double-sided seeding to the worst interferometer performance (largest f_{PFS}) due to the presence of the ‘‘pair term’’ $\bar{N}_{+1}\bar{N}_{-1}$ in Eq. (47). Importantly though, even initial balanced double-sided seeding improves the interferometer performance compared to that for the vacuum state.

TABLE III. Explicit expressions for $\min(\Delta\theta_{\text{ep,VS}})$ [Eq. (54)] and the associated $(\theta_{\text{min}})_{\text{VS}}$ [Eq. (55)] for the resonant symmetric interferometer, resonant asymmetric interferometer, and non-resonant symmetric interferometer. The results are obtained within the undepleted pump approximation.

	resonant symmetric	resonant asymmetric	non-resonant symmetric
$(\theta_{\text{min}})_{\text{VS}}$	π	$\arccos[-\tanh(2\min(\xi_1, \xi_3)) \coth(2\max(\xi_1, \xi_3))] + \gamma_{B_1} - \gamma_{B_3}$	$\pi + 2\gamma_A$
$\min(\Delta\theta_{\text{ep,VS}})$	$\text{csch}(2\xi)$	$\text{csch}[2\min(\xi_1, \xi_3)]$	$\left \frac{ A ^2 - B ^2}{2AB} \right $

We now analyze $\Delta\theta_{\text{ep,VS}}$. Due to the sin and cos dependence of $\Delta\theta_{\text{ep,VS}}$, this quantity has a reflection symmetry around $\theta = \pi + \gamma_{A_1} + \gamma_{A_3} + \gamma_{B_1} - \gamma_{B_3}$. Minimizing $\Delta\theta_{\text{ep,VS}}$ with respect to θ yields the best possible interferometer performance for the SU(1,1) interferometer with pure Fock state input. We find

$$\min(\Delta\theta_{\text{ep,VS}}) = \sqrt{\frac{s + t + \sqrt{s(s + 2t + 2u)}}{u}} \quad (54)$$

for

$$(\theta_{\text{min}})_{\text{VS}} = \arccos\left(-\frac{s + t + u - \sqrt{s(s + 2t + 2u)}}{t + u}\right) + \gamma_{A_1} + \gamma_{A_3} + \gamma_{B_1} - \gamma_{B_3}. \quad (55)$$

Table III summarizes explicit expressions for $\min(\Delta\theta_{\text{ep,VS}})$ and $(\theta_{\text{min}})_{\text{VS}}$ for the resonant symmetric, resonant asymmetric, and non-resonant symmetric SU(1,1) interferometers. For symmetric interferometers,

the best performance (minimum of $\Delta\theta_{\text{ep,VS}}$) is reached for $\theta = \pi + 2\gamma_A$, i.e., the angle about which $\Delta\theta_{\text{ep,VS}}$ has a reflection symmetry. The solid line in Fig. 4 illustrates this for the resonant symmetric interferometer with $\xi_1 = \chi_1 = \xi_3 = \chi_3 = 1$ ($\gamma_A = 0$ and $\gamma_{B_1} = \gamma_{B_3} = -\pi/2$), implying that the best performance is reached for $\theta = \pi$. In this case, the minimum of the error propagation based phase sensitivity coincides with the quantum Cramer-Rao bound (horizontal green solid line in Fig. 4), which lies below the standard quantum limit and below the Heisenberg limit (horizontal green dashed and dotted lines in Fig. 4). This implies that the Heisenberg limit does, in this case, not provide a stringent lower bound. The quantum Cramer-Rao bound is also reached for the non-resonant asymmetric interferometer with $\xi_1 = \chi_1 = 1$, $\xi_3 = 3/2$, and $\chi_3 = 0$ (blue dash-dotted line); in this case, however, the minimum of the error propagation based sensitivity is reached at a different angle, namely at $\theta = 0.624\pi$ and 0.75π . Returning

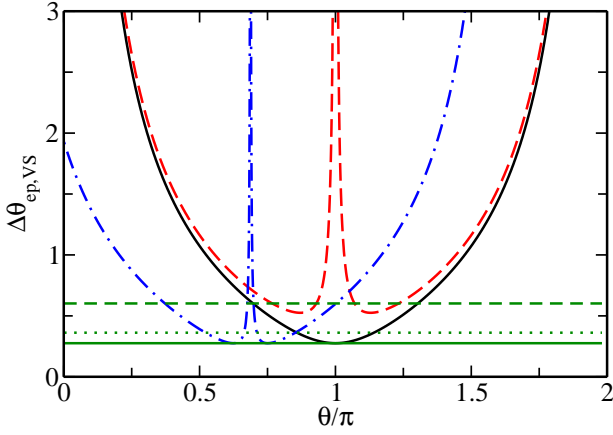


FIG. 4. (Color online) $\Delta\theta_{\text{ep,VS}}$ as a function of θ for three interferometers that are characterized by the same ξ_1 and χ_1 (namely, $\xi_1 = \chi_1 = 1$) but different ξ_3 and χ_3 for the case where the initial state is the vacuum state $|0, \bar{N}_0, 0\rangle$. The black solid curve is for a resonant symmetric interferometer with $\xi_3 = \chi_3 = 1$, the blue dash-dotted line is for a non-resonant asymmetric interferometer with $\xi_3 = 3/2$ and $\chi_3 = 0$, and the red dashed line is for a resonant asymmetric interferometer with $\xi_3 = 7/10$ and $\chi_3 = 1$. The minimum of the phase sensitivity of the two former interferometers is the same but the minimal value is reached at different angles. The quantum Cramer-Rao bound $\Delta\theta_{\text{QCR}}$ (horizontal green solid line), the standard quantum limit $[N_s(t_1)]^{-1/2}$ (horizontal green dashed line), and the Heisenberg limit $[N_s(t_1)]^{-1}$ (horizontal green dotted line) are the same for all three interferometers.

to the asymmetric interferometer but considering the resonant case with $\xi_1 = \chi_1 = \chi_3 = 1$ and $\xi_3 = 7/10$ (red dashed line), we see that the minimum of the error propagation based phase sensitivity lies above that of the resonant symmetric interferometer with $\xi_3 = 1$. In fact, for pure Fock states the minimum of the error propagation based phase sensitivity for the resonant

interferometer decreases monotonically with increasing ξ_3 for $\xi_3 < \xi_1$ and then takes a constant value for $\xi_3 > \xi_1$ [see the black solid and blue dashed lines in Fig. 6(a)].

With the properties of the quantities f_{PFS} and $\Delta\theta_{\text{ep,VS}}$ mapped out, we compare the minimum of the phase sensitivity $\Delta\theta_{\text{ep,PFS}}$ and the corresponding quantum Cramer-Rao bound, i.e., we calculate the ratio

$$\frac{\min(\Delta\theta_{\text{ep,PFS}})}{\Delta\theta_{\text{QCR,PFS}}} = \frac{\min(\Delta\theta_{\text{ep,VS}})}{\Delta\theta_{\text{QCR,VS}}} \left(1 + \frac{2\bar{N}_{+1}\bar{N}_{-1}}{1 + \bar{N}_s}\right). \quad (56)$$

We do not have a general result for when this equation is equal to one and when it is greater than one. In the parameter range $0 < q_j/q_{c,j} < 2$, however, a sufficient condition for the prefactor $\min(\Delta\theta_{\text{ep,VS}})/\Delta\theta_{\text{QCR,VS}}$ being equal to one is $\xi_3 \geq \xi_1$ and $\chi_3 \geq \chi_1$. Thus, in this parameter regime (which includes a variety of non-resonant asymmetric interferometers), a pure Fock state without seeding or with single-sided seeding does reach the quantum Cramer-Rao bound while a pure Fock state with double-sided seeding does not reach the quantum Cramer-Rao bound.

B. Coherent spin state

Let the initial state be a coherent spin state (CSS) [20]. Generally speaking, coherent spin states with single- and double-sided seeding are much easier to prepare experimentally than pure Fock states with seeding. Coherent spin states may be characterized as the most classical of all quantum states [36]. Thus, intuitively one might expect that coherent spin states perform less well than pure Fock states for the same interferometer parameters during steps 1. and 3. of the interferometer sequence. This section shows that coherent spin states with double-sided seeding yield, in some cases, a smaller error propagation based phase sensitivity than pure Fock states.

Our analytical results within the undepleted pump approximation are derived for the coherent spin state

$$|\beta_{+1}, \beta_{-1}\rangle = \sum_{n_{+1}=0}^{\infty} \sum_{n_{-1}=0}^{\infty} \exp\left(-\frac{|\beta_{+1}|^2 + |\beta_{-1}|^2}{2}\right) \frac{(\beta_{+1})^{n_{+1}} (\beta_{-1})^{n_{-1}}}{\sqrt{n_{+1}! n_{-1}!}} |n_{+1}, n_{-1}\rangle, \quad (57)$$

where the complex numbers β_m are written in terms of the initial atoms \bar{N}_m in the side modes and the initial phases $\bar{\theta}_m$ of the $m = +1$ and $m = -1$ modes, $\beta_m = (\bar{N}_m)^{1/2} \exp(i\bar{\theta}_m)$. A derivation of this state is given in Appendix C. Consistent with the fact that \hat{H}_{UPA} does not conserve the number of particles, this “two-mode” state ($|n_{+1}, n_{-1}\rangle$ denotes a Fock state) is characterized by a distribution of number of atoms. The relative phase $\bar{\theta}$,

$$\bar{\theta} = -(\bar{\theta}_{+1} + \bar{\theta}_{-1}), \quad (58)$$

of the state given in Eq. (57) is well-defined in the case of double-sided seeding but not in the case of single-sided seeding or without seeding; the latter is equal to the vacuum state. In the case of initial double-sided seeding, the interferometer performance depends on the relative phase, thereby providing another tuning knob.

For the initial coherent spin state given in Eq. (57), Eqs. (34) and (35) reduce to

$$N_s(t_1 + t_2 + t_3) = |\tilde{A}|^2 + |\tilde{B}|^2 - 1 + 2|\tilde{A}\tilde{B}| \left[\mathcal{I} \bar{N}_s + 2g(\bar{\theta}, \gamma_{\tilde{A}}, -\gamma_{\tilde{B}}) \sqrt{\bar{N}_{+1}\bar{N}_{-1}} \right] \quad (59)$$

and

$$\Delta N_s(t_1 + t_2 + t_3) = 2|\tilde{A}\tilde{B}| \sqrt{1 + (1 + \mathcal{I}^2) \bar{N}_s + 4\mathcal{I}g(\bar{\theta}, \gamma_{\tilde{A}}, -\gamma_{\tilde{B}}) \sqrt{\bar{N}_{+1}\bar{N}_{-1}}}, \quad (60)$$

respectively, where the function $g(\bar{\theta}, \gamma_{\tilde{A}}, -\gamma_{\tilde{B}})$ is equal to zero when $\bar{\theta}$ is not well defined (coherent spin state without seeding or with single-sided seeding) and $g(\bar{\theta}, \gamma_{\tilde{A}}, -\gamma_{\tilde{B}}) = \cos(\bar{\theta} - \gamma_{\tilde{A}} + \gamma_{\tilde{B}})$ when $\bar{\theta}$ is well defined (coherent spin state with double-sided seeding). In the case of an initial state with double-sided seeding, the function $g(\bar{\theta}, \gamma_{\tilde{A}}, -\gamma_{\tilde{B}})$ “mixes” the properties of the initial state (through $\bar{\theta}$) and the actual device (through $\gamma_{\tilde{A}}$ and $\gamma_{\tilde{B}}$).

The next two sections separately discuss the interferometer performance within the undepleted pump approximation for coherent spin states with single- and double-sided seeding. We have checked that our analytical results presented in the next two sections agree, up to terms of order $1/N$, with the numerical results for the full spin Hamiltonian \hat{H}_{spin} . To make the comparisons, we used an initial coherent spin state with fixed particle number [Eq. (C1)] in our exact diagonalization.

1. Coherent spin state with single-sided seeding

For an initial coherent spin state with single-sided seeding, $N_s(t)$ is, for the same interferometer parameters, identical to that for a pure Fock state with single-sided seeding [compare Eq. (59) with Eq. (43)]. The quantum fluctuation $\Delta N_s(t)$ for the coherent spin state with single-sided seeding, in contrast, differs from that for a pure Fock state with single-sided seeding since \mathcal{I} is, in general, non-zero [compare Eq. (60) with Eq. (44)]. Correspondingly, the phase sensitivity for the coherent spin state with single-sided seeding also differs from that for the pure Fock state with single-sided seeding. We find

$$\Delta\theta_{\text{ep,CSS,S}} = \Delta\theta_{\text{ep,VS}} f_{\text{CSS,S}}, \quad (61)$$

where

$$f_{\text{CSS,S}} = \frac{\sqrt{1 + (1 + \mathcal{I}^2) \bar{N}_s}}{1 + \bar{N}_s}. \quad (62)$$

For $\bar{N}_s = 0$, Eq. (61) reduces to $\Delta\theta_{\text{ep,VS}}$; this is in agreement with the fact that the coherent spin state without seeding reduces to the vacuum state. The factor $f_{\text{CSS,S}}$ depends on the initial state through \bar{N}_s and the actual device through \mathcal{I} . The \mathcal{I}^2 term in round brackets under the square root in Eq. (62) leads, for the same interferometer parameters, to a degradation of the best interferometer performance for an initial coherent spin state

with single-sided seeding compared to that of a pure Fock state with single-sided seeding [compare Eq. (62) with Eq. (47)]. Importantly, the factor $f_{\text{CSS,S}}$ can take values smaller than 1. This implies that a coherent spin state with single-sided seeding can—for the same interferometer parameters—perform better than an initial vacuum state.

Since $\Delta\theta_{\text{ep,VS}}$ and $f_{\text{CSS,S}}$ both depend explicitly on θ , determining the best interferometer performance requires that one minimizes the product $\Delta\theta_{\text{ep,VS}} f_{\text{CSS,S}}$, i.e., the two terms cannot be treated separately. This differs from the pure Fock state case considered in Sec. IV A, where $\Delta\theta_{\text{ep,VS}}$ and f_{PFS} could be minimized separately. While the minimization of $\Delta\theta_{\text{ep,VS}} f_{\text{CSS,S}}$ can, in principle, be done analytically, the resulting expression for the minimum of the error propagation based phase sensitivity is rather lengthy and not overly illuminating. The following examples illustrate selected characteristics of the interferometer performance for coherent spin states with single-sided seeding.

The minimum and maximum of \mathcal{I} are reached at $\theta = \gamma_{A_1} + \gamma_{A_3} + \gamma_{B_1} - \gamma_{B_3}$ and $\theta = \pi + \gamma_{A_1} + \gamma_{A_3} + \gamma_{B_1} - \gamma_{B_3}$, respectively,

$$\min \mathcal{I}|_{\theta=\gamma_{A_1}+\gamma_{A_3}+\gamma_{B_1}-\gamma_{B_3}} = \frac{t + 2u}{\sqrt{2u(s + 2t + 2u)}} \quad (63)$$

and

$$\max \mathcal{I}|_{\theta=\pi+\gamma_{A_1}+\gamma_{A_3}+\gamma_{B_1}-\gamma_{B_3}} = \frac{t}{\sqrt{2us}}. \quad (64)$$

Correspondingly, for fixed \bar{N}_s , $f_{\text{CSS,S}}$ takes its minimum and maximum at these angles. It is easy to check that the θ dependence in $f_{\text{CSS,S}}$ and $\Delta\theta_{\text{ep,VS}}$ enters only through $\cos(\theta - \gamma_{A_1} - \gamma_{A_3} - \gamma_{B_1} + \gamma_{B_3})$. Correspondingly, $f_{\text{CSS,S}}$ and $\Delta\theta_{\text{ep,VS}}$ have a reflection symmetry around $\theta = \pi + \gamma_{A_1} + \gamma_{A_3} + \gamma_{B_1} - \gamma_{B_3}$. For this angle, the seeding factor $f_{\text{CSS,S}}$ diverges for symmetric interferometers and the phase sensitivity $\Delta\theta_{\text{ep,VS}}$ diverges for asymmetric interferometers. Thus, $\Delta\theta_{\text{ep,CSS,S}}$ diverges at this angle for all interferometers. This is consistent with the fact that ΔN_s is finite and $\partial_\theta N_s$ is zero for $\theta = \pi + \gamma_{A_1} + \gamma_{A_3} + \gamma_{B_1} - \gamma_{B_3}$.

As an example, the black solid lines in Figs. 5(a) and 5(b) show $\Delta\theta_{\text{ep,CSS,S}}$ for, respectively, a resonant symmetric and a resonant asymmetric interferometer for an initial coherent spin state with single-sided seeding

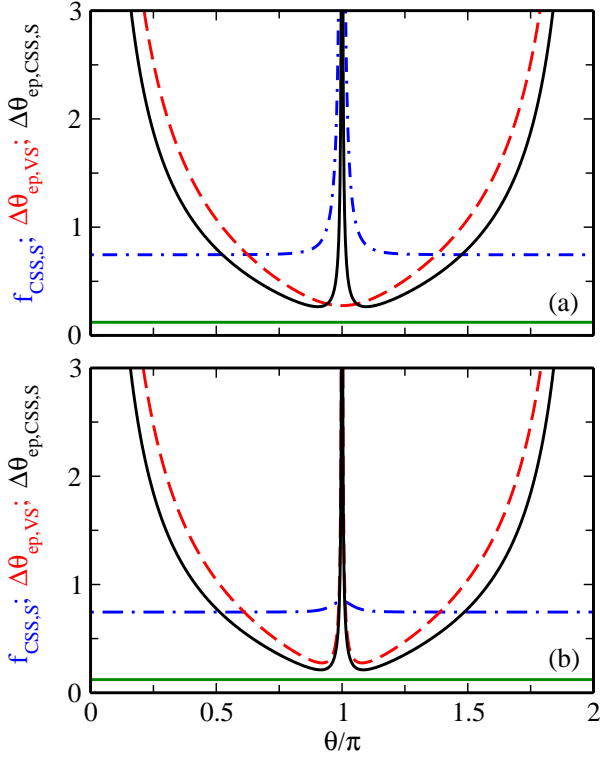


FIG. 5. (Color online) Analysis of the phase sensitivity for a coherent spin state with single-sided seeding ($\overline{N}_s = 2$) as a function of θ for a resonant interferometer with $\chi_1 = \chi_3 = 1$ ($\gamma_{A_1} = \gamma_{A_3} = 0$ and $\gamma_{B_1} = \gamma_{B_3} = -\pi/2$). (a) Results for the resonant symmetric interferometer with $\xi_1 = \xi_3 = 1$. (b) Results for the resonant asymmetric interferometer with $\xi_1 = 1$ and $\xi_3 = 3/2$. The red dashed lines show $\Delta\theta_{\text{ep,VS}}$ while the blue dash-dotted lines show $f_{\text{CSS,S}}$. The product of these two quantities yields the phase sensitivity $\Delta\theta_{\text{ep,CSS,S}}$ (black solid lines). The horizontal green solid lines show the quantum Cramer-Rao bound.

($\overline{N}_s = 2$). Since γ_{A_1} and γ_{A_3} are equal to zero for resonant interferometers, the reflection symmetry and divergence points of $\Delta\theta_{\text{ep,CSS,S}}$ are located at $\theta = \pi$. For the resonant symmetric interferometer in Fig. 5(a), the fact that \mathcal{I} is minimized at the angle at which $\Delta\theta_{\text{ep,VS}}$ is maximized and that \mathcal{I} diverges at the angle at which $\Delta\theta_{\text{ep,VS}}$ is minimized highlights that the quantities $\Delta\theta_{\text{ep,VS}}$ and $f_{\text{CSS,S}}$ “compete” when minimizing $\Delta\theta_{\text{ep,CSS,S}}$. As a consequence, the smallest phase sensitivity is reached when neither $f_{\text{CSS,S}}$ nor $\Delta\theta_{\text{ep,VS}}$ are minimized, namely at $(\theta_{\text{min}})_{\text{CSS,S}} = 0.904\pi$ and 1.096π for the example shown in Fig. 5(a). For the resonant asymmetric interferometer in Fig. 5(b), $\Delta\theta_{\text{ep,VS}}$ and $f_{\text{CSS,S}}$ take their maximum at $\theta = \pi$. The minimum of $\Delta\theta_{\text{ep,CSS,S}}$ is lower than that of $\Delta\theta_{\text{ep,VS}}$ but located, roughly, at the same angle.

The examples in Fig. 5 show that an initial coherent spin state with single-sided seeding can improve the interferometer performance compared to an initial vacuum state. While the minimum of the error propagation based phase sensitivity for the coherent spin state with single-sided seeding is, for the examples shown in Fig. 5, larger

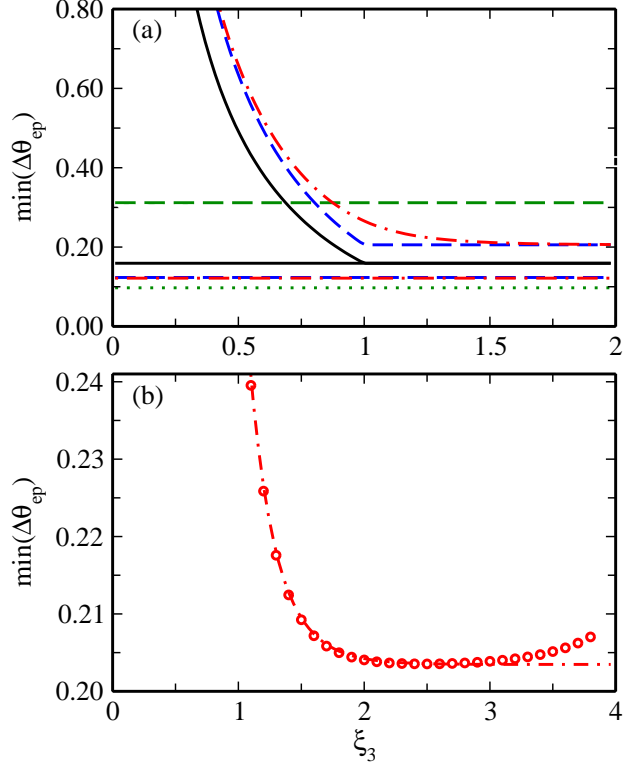


FIG. 6. (Color online) (a) Minimum of the phase sensitivity $\Delta\theta_{\text{ep}}$ for three different initial states with $\overline{N}_s = 2$ for the resonant interferometer with $\xi_1 = \chi_1 = \chi_3 = 1$ as a function of ξ_3 . Results are shown for the pure Fock state with single-sided seeding (black solid line), pure Fock state with double-sided seeding (blue dashed line), and coherent spin state with single-sided seeding (red dash-dotted line). The three cases share the same standard quantum limit (horizontal green dashed line) and the same Heisenberg limit $\Delta\theta_{\text{HL}}$ (horizontal green dotted line). The quantum Cramer-Rao bound $\Delta\theta_{\text{QCR}}$ for the pure Fock state with single-sided seeding (horizontal black solid line), the pure Fock state with double-sided seeding (horizontal blue dashed line), and the coherent spin state with single-sided seeding (horizontal red dash-dotted line) all lie above the Heisenberg limit $\Delta\theta_{\text{HL}}$ (note that the horizontal blue dashed and red dash-dotted lines nearly coincide). (b) The symbols show the minimum $\min(\Delta\theta_{\text{ep,CSS,S}})$ of the phase sensitivity, obtained by numerically determining the time evolution for the full spin Hamiltonian for a ^{23}Na condensate with $N = 10000$, for the coherent spin state with single-sided seeding ($\overline{N}_s = 2$). The red dash-dotted line from panel (a) is reproduced for comparison. The deviations between the symbols and the dash-dotted line for $\xi_3 \gtrsim 3$ reflect the breakdown of the undepleted pump approximation in the long-time regime.

than the quantum Cramer-Rao bound (horizontal green solid line), it is smaller than the quantum Cramer-Rao bound for the vacuum state (not shown in Fig. 5).

To highlight the dependence of the minimum of the phase sensitivity $\Delta\theta_{\text{ep}}$ on the initial state, Fig. 6(a) considers the resonant interferometer with $\chi_1 = \chi_3 = \xi_1 = 1$

as a function of ξ_3 for three different initial states: pure Fock state with single-sided seeding (black solid line), pure Fock state with double-sided seeding (blue dashed line), and coherent spin state with single-sided seeding (red dash-dotted line). For $\xi_3 < \xi_1$, all three curves decrease monotonically with increasing ξ_3 , with $\Delta\theta_{\text{ep,CSS,S}} > \Delta\theta_{\text{ep,PFS,D}} > \Delta\theta_{\text{ep,PFS,S}}$ at each fixed ξ_3 . The phase sensitivities for the two pure Fock states are constant for $\xi_3 > \xi_1$. For the coherent spin state, in contrast, the minimum of the phase sensitivity for $\xi_3 > \xi_1$ continues to decrease and approaches a constant in the $\xi_3 \rightarrow \infty$ limit. We emphasize that the decrease of $\Delta\theta_{\text{ep}}$ for $\xi_3 \gtrsim \xi_1$ is reproduced by our numerical calculations for the full spin Hamiltonian for a ^{23}Na BEC with $N = 10000$ [symbols in Fig. 6(b)]. However, for $\xi_3 \gg \xi_1$ the phase sensitivity obtained for the full spin Hamiltonian deviates from the results obtained within the undepleted pump approximation, underscoring the fact that the long-time dynamics is not described faithfully by the undepleted pump approximation.

Interestingly, the quantum Cramer-Rao bound for the three states considered in Fig. 6(a) all lie above the

Heisenberg limit (horizontal green dotted line). This implies that the Heisenberg limit lies, in this case, below the fundamental bound, i.e., the Heisenberg limit can never be reached.

2. Coherent spin state with double-sided seeding

This section considers the interferometer performance for an initial coherent spin state with double-sided seeding. Compared to the coherent spin state with single-sided seeding, the relative phase $\bar{\theta}$ and the distribution of the atoms among the two probe modes (i.e., the product $\bar{N}_+\bar{N}_-$) provide additional tuning knobs.

For an initial coherent spin state with double-sided seeding, the error propagation based phase sensitivity can be written as

$$\Delta\theta_{\text{ep,CSS,D}} = \Delta\theta_{\text{ep,VS}} f_{\text{CSS,D}}, \quad (65)$$

where

$$f_{\text{CSS,D}} = \frac{\sqrt{1 + (1 + \mathcal{I}^2) \bar{N}_s + 4\mathcal{I} \cos(\bar{\theta} - \gamma_{\bar{A}} + \gamma_{\bar{B}}) \sqrt{\bar{N}_{+1}\bar{N}_{-1}}}}{\left| 1 + \bar{N}_s + [2\mathcal{I} \cos(\bar{\theta} - \gamma_{\bar{A}} + \gamma_{\bar{B}}) + 2\Delta\theta_{\text{ep,VS}} \sin(\bar{\theta} - \gamma_{\bar{A}} + \gamma_{\bar{B}}) \partial_{\theta}(\gamma_{\bar{B}} - \gamma_{\bar{A}})] \sqrt{\bar{N}_{+1}\bar{N}_{-1}} \right|}. \quad (66)$$

It can be readily checked that $f_{\text{CSS,D}}$ reduces to $f_{\text{CSS,S}}$ if $\bar{N}_+\bar{N}_-$ is equal to zero. For non-zero $\bar{N}_+\bar{N}_-$ and fixed interferometer parameters, the terms in the numerator and denominator of Eq. (66) that contain $\bar{N}_+\bar{N}_-$ take, depending on the value of $\bar{\theta} - \gamma_{\bar{A}} + \gamma_{\bar{B}}$, positive or negative values: The quantities \mathcal{I} and $\Delta\theta_{\text{ep,VS}}$ are positive for all interferometer parameters; $\partial_{\theta}(\gamma_{\bar{B}} - \gamma_{\bar{A}})$ and the sin- and cos-terms, in contrast, can take positive or negative values.

To illustrate the interplay of the different terms that enter into $\Delta\theta_{\text{ep,CSS,D}}$, we consider the resonant asymmetric interferometer with $\chi_1 = \chi_3 = \xi_1 = 1$ and $\xi_3 = 3/2$. The dashed, dash-dotted, and solid lines in Fig. 7(a) show the quantities $\Delta\theta_{\text{ep,VS}}$, \mathcal{I} , and $\partial_{\theta}(\gamma_{\bar{B}} - \gamma_{\bar{A}})$ as a function of θ . These quantities are fully determined by the interferometer parameters, i.e., they are independent of the initial state. As already discussed in the context of Fig. 5, $\Delta\theta_{\text{ep,VS}}$ exhibits minima for θ just a bit larger and just a bit smaller than π . For these angles, \mathcal{I} and $\partial_{\theta}(\gamma_{\bar{B}} - \gamma_{\bar{A}})$ take “intermediate” values (not maxima and not minima). Since $\Delta\theta_{\text{ep,CSS,D}}$ is directly proportional to $\Delta\theta_{\text{ep,VS}}$ and since $\Delta\theta_{\text{ep,VS}}$ also enters through the denominator of $f_{\text{CSS,D}}$, $\Delta\theta_{\text{ep,CSS,D}}$ possesses a non-trivial dependence on θ .

Choosing the balanced case with $\bar{N}_+/\bar{N}_- = 1$ as an example, Fig. 7(b) shows $f_{\text{CSS,D}}$ as a function of the phase

shifter angle θ for various initial phases $\bar{\theta}$ of the coherent spin state. It can be seen that $f_{\text{CSS,D}}$ depends strongly on θ and $\bar{\theta}$: $f_{\text{CSS,D}}$ changes by roughly four orders of magnitude for $\bar{\theta} = 0.36\pi$ and $\bar{\theta} = 0$ and by less than an order of magnitude for $\bar{\theta} = \pi/2$. For the example shown, $f_{\text{CSS,D}}$ takes a minimum at $\theta = \pi$ (for all $\bar{\theta}$ considered) and a local minimum at $\theta = 0$ and 2π (for all $\bar{\theta}$ considered except for $\bar{\theta} = \pi/2$). These are exactly the angles at which $\Delta\theta_{\text{ep,VS}}$ diverges. Figure 7(c) shows the error propagation based phase sensitivity $\Delta\theta_{\text{ep,CSS,D}}$ for the same initial phases $\bar{\theta}$ as considered in Fig. 7(b). It can be seen that the minimum of $\Delta\theta_{\text{ep,CSS,D}}$ is obtained for θ close to but not equal to π .

Repeating the analysis for other \bar{N}_+/\bar{N}_- , Fig. 8 shows the minimum $\min(\Delta\theta_{\text{ep,CSS,D}})$ of the phase sensitivity as functions of $\bar{\theta}$ and \bar{N}_+/\bar{N}_- for the same interferometer parameters as considered in Fig. 7. For $\bar{N}_+/\bar{N}_- = 0$, $\min(\Delta\theta_{\text{ep,CSS,D}})$ is independent of $\bar{\theta}$ and equal to 0.2120; this value agrees, as it should, with the minimum of the error propagation based phase sensitivity for the coherent spin state with single-sided seeding (see the dash-dotted line in Fig. 6 for $\xi_3 = 3/2$). Figure 8 shows that the minimum $\min(\Delta\theta_{\text{ep,CSS,D}})$ of the error propagation based phase sensitivity can, depending on the values of \bar{N}_+/\bar{N}_- and $\bar{\theta}$, be larger or smaller than $\min(\Delta\theta_{\text{ep,CSS,S}})$.

It is interesting to compare the performance of the ini-

tial coherent spin state with double-sided seeding with that for the initial pure Fock state with single-sided seeding (and the same \overline{N}_s); recall, among the pure Fock states, the pure Fock state with single-sided seeding yields the smallest phase sensitivity $\Delta\theta_{\text{ep}}$ for fixed interferometer parameters. For the interferometer parameters considered in Fig. 8, the smallest phase sensitivity for the pure Fock state is equal to 0.1592. Thus, the minimum of the phase sensitivity for the initial coherent spin state with double-sided seeding is, for a range of $\overline{\theta}$ and $\overline{N}_+/\overline{N}_-$, smaller than that for the pure Fock state with single-sided seeding. This result is very encouraging as it points toward the possibility of achieving comparable or even better phase or parameter estimates for initial coherent spin states with double-sided seeding, which are experimentally fairly straightforward to prepare, than for initial pure Fock states with single-sided seeding, which are experimentally rather challenging to prepare.

The solid line in Fig. 9 shows the minimum of the error propagation based phase sensitivity for an initial coherent spin state with $\overline{N}_s = 2$ for the resonant interferometer with $\chi_1 = \chi_3 = \xi_1 = 1$ as a function of ξ_3 . In this analysis, the minimum of the phase sensitivity is obtained by minimizing $\Delta\theta_{\text{ep,CSS,D}}$ with respect to $\overline{\theta}$ and $\overline{N}_+/\overline{N}_-$ as well as the angle θ . For comparison, the dashed line shows the quantum Cramer-Rao bound, calculated for each ξ_3 using the $\overline{\theta}$ and $\overline{N}_+/\overline{N}_-$ values that yield the smallest $\Delta\theta_{\text{ep,CSS,D}}$. It can be seen that the error propagation based phase sensitivity is closest to the quantum Cramer-Rao bound for the largest ξ_3 considered, i.e., for $\xi_3 = 2$. By analyzing the dynamics for the full spin Hamiltonian for a ^{23}Na BEC with $N = 10000$, we checked that the undepleted pump approximation provides an accurate description for all ξ_3 values considered in Fig. 9. It is also instructive to compare with the quantum Cramer-Rao bounds for the double-sided and single-sided pure Fock states, which are equal to 0.1233 and 0.1592, respectively, for $\xi_3 \geq 1$. We find that the error propagation based phase sensitivity for the coherent spin state is lower than the quantum Cramer-Rao bound for the pure Fock state for the same interferometer parameters for $\xi_3 > 1.280$ and $\xi_3 > 1.054$, respectively. This is interesting, since it indicates that the performance of the SU(1,1) interferometer, as quantified by the error propagation based phase sensitivity, can “beat” the quantum Cramer-Rao bound for the pure Fock state, assuming the same initial seeding \overline{N}_s and the same interferometer parameters.

V. CONCLUSIONS

This work analyzed the performance of a spin-1 Bose-Einstein condensate based interferometer for parameter combinations that can be realized experimentally. Within the undepleted pump approximation, which is employed throughout this paper, the spinor BEC realizes an SU(1,1) interferometer, in which the $m = 0$ state of

the $f = 1$ hyperfine manifold serves as the pump and the $m = +1$ and $m = -1$ hyperfine states serve as the probe. Although the interferometer itself, which consists of the state preparation, phase imprinting, and read-out steps, has eight experimentally tunable parameters ($t_1, q_1, c_1, t_2, q_{\text{ps}}, t_3, q_3, c_3$), it is characterized by five parameters within the undepleted pump approximation: two that describe the state preparation step, one that describes the phase imprinting step, and two that describe the read-out step. The initial state adds additional degrees of freedom: For pure Fock states the fraction of atoms in the three different hyperfine states can be varied. For coherent spin states with double-sided seeding, the initial relative phase provides an additional tuning knob. The validity regime of the undepleted pump approximation limited our analysis to cases where the side mode population of the initial state and the time propagated state are much smaller than the population of the pump mode.

The dependence of the performance of the spinor-BEC based SU(1,1) interferometer on the seeding fraction and initial phase of coherent spin states was already investigated in Ref. [35] within the truncated Wigner approximation. As in our work, both phase insensitive amplifiers (single-sided seeding) and phase sensitive amplifiers (double-sided seeding) were considered. Our analytical results, obtained within the undepleted pump approximation, confirm the results of Ref. [35] with regards to the role played by the initial state: (ai) Even a tiny seeding fraction has a non-negligible effect on the interferometer performance; correspondingly, an analysis of experimental interferometer results needs to account for possible imperfections of the initial state. (aii) The best interferometer performance $\min(\Delta\theta_{\text{ep}})$ of a coherent spin state with single-sided seeding is obtained for a phase shifter angle that differs (typically just slightly) from that of the vacuum state; in fact, the angle at which the vacuum state performs best yields the worst performance for the coherent spin state with single-sided seeding. For the same interferometer parameters, an initial coherent spin state with single-sided seeding yields a lower $\min(\Delta\theta_{\text{ep}})$ than an initial vacuum state. (aiii) The coherent spin state with double-sided seeding can perform better than the vacuum state and pure Fock states with single- and double-sided seeding for appropriately chosen initial phases. This is a very encouraging result from the experimental point of view since coherent spin states with double-sided seeding can be realized fairly straightforwardly by first preparing a condensate in the $|f = 1, m = 0\rangle$ state and by then applying a short radio-frequency pulse that transfers a fraction of the atoms into the $m = \pm 1$ states. The initial phases of the three hyperfine components can be controlled by introducing a finite variable detuning. Alternatively, microwave transitions that couple to the $f = 2$ manifold can be used [24, 26, 27].

Additional findings of our work are: (bi) Within the undepleted pump approximation, analytical expressions that account for all three steps of the SU(1,1) interferometer sequence were presented for an arbitrary pure initial

state and analyzed for a subset of Fock and coherent spin states. We expect that these expressions, which can be straightforwardly implemented in Mathematica or other software packages, will aid the analysis of experimental results and serve as a benchmark for solutions that go beyond the undepleted pump approximation. (bii) Pure Fock states with single-sided seeding perform, assuming the same interferometer parameters, better than pure Fock states with double-sided seeding. Pure Fock states with double-sided seeding, in turn, perform better than the vacuum state. From a practical point of view, pure Fock states with non-zero seeding are rather fragile and hence challenging to work with experimentally. (biii) Parameter regimes where coherent spin states perform better than pure Fock states with single-sided seeding, in addition to performing better than the vacuum state [see point (aiii) above], were identified (again, assuming the same interferometer parameters). This is encouraging since this finding underscores that the spin mixing dynamics can generate, starting from an initial coherent state that may be viewed as the most classical of all quantum states, useful “quantum-ness” or entanglement during the first stage of the interferometer sequence.

Last, we highlight a number of key findings that relate to the interferometer steps themselves. (ci) For a coherent spin state with single- or double-sided seeding, the error propagation based sensitivity continues, for a wide range of parameters, to decrease for $\xi_3 > \xi_1$, i.e., when $t_3 > t_1$. This asymmetric behavior might be enhanced if one goes beyond the undepleted pump approximation. (cii) The quantum Cramer-Rao bound, which is fully determined by the state $|\Psi(t_1)\rangle$ that enters the linear phase imprinting step of the interferometer, provides the ultimate lower bound for the phase sensitivity; unfortunately, however, no general protocols for its direct experimental determination exist. The error propagation based phase sensitivity $\Delta\theta_{\text{ep}}$, in contrast, depends on all three stages of the interferometer. Our calculations suggest that it is, in general, not possible to predict $\min(\Delta\theta_{\text{ep}})$ by simply maximizing $N_s(t_1)$ or $\Delta N_s(t_1)$. While this is not unexpected, it highlights the interconnectedness of the various parameters. (ciii) The Heisenberg limit [taken to be given by $1/N_s(t_1)$] lies, for certain parameter combinations, below the quantum Cramer-Rao bound, indicating that one should, in general, work with the quantum Cramer-Rao bound and not with the Heisenberg limit. Since the observed behavior was verified by performing calculations for the full spin Hamiltonian, this conclusion is not an artifact of the undepleted pump approximation but valid more generally.

ACKNOWLEDGEMENT

We gratefully acknowledge discussions with Arne Schwettmann, Qimin Zhang, and Shan Zhong. Support by the National Science Foundation through grant number PHY-1806259 is gratefully acknowledged. This work

used the OU Supercomputing Center for Education and Research (OSKER) at the University of Oklahoma (OU).

Appendix A: GP equation

According to Eq. (3), the strength c of the collision term in the spin Hamiltonian is determined by \bar{c} and \bar{n} . For ^{23}Na , e.g., a_0 and a_2 are $48.91 a_{\text{bohr}}$ and $54.54 a_{\text{bohr}}$ [37] (a_{bohr} denotes the Bohr radius), respectively, leading to $\bar{c}/\hbar = 1.54 \times 10^{-17} \text{ Hz m}^3$. To determine the mean spatial density \bar{n} , we treat a single-component ^{23}Na BEC within the mean-field Gross-Pitaevskii framework. To this end, we solve the Gross-Pitaevskii equation

$$\left[-\frac{\hbar^2}{4\mu} \nabla_{\vec{r}}^2 + \mu(\omega_x^2 x^2 + \omega_y^2 y^2 + \omega_z^2 z^2) + \frac{2\pi\hbar^2(N-1)(a_0 + 2a_2)}{3\mu} |\psi_{\text{GP}}(\vec{r})|^2 \right] \psi_{\text{GP}}(\vec{r}) = \epsilon \psi_{\text{GP}}(\vec{r}), \quad (\text{A1})$$

where ϵ denotes the chemical potential and $\psi_{\text{GP}}(\vec{r})$ the mean-field orbital, which we take to be normalized to 1. Given $\psi_{\text{GP}}(\vec{r})$, the mean density \bar{n} is given by

$$\bar{n} = N \int |\psi_{\text{GP}}(\vec{r})|^4 d\vec{r}. \quad (\text{A2})$$

For an external harmonic trap with angular frequencies $\omega_x = \omega_y = 2\pi \times 166.277 \text{ Hz}$ and $\omega_z = 2\pi \times 216.498 \text{ Hz}$, we find $\bar{n} = 1.04 \times 10^{18} \text{ m}^{-3}$, $c_j/\hbar = 15.9956 \text{ Hz}$ and $q_{c,j}/\hbar = -15.9948 \text{ Hz}$ for a ^{23}Na condensate with $N = \bar{N}_0 = 10000$. These are the values that are used to obtain the results for \hat{H}_{spin} shown in Figs. 2, 3, and 6(b). We emphasize that the results obtained within the undepleted pump approximation employ dimensionless parameters. This implies that the undepleted pump approximation results shown in Figs. 3-9 are applicable to a wide range of atomic species. The main limitation is that the sign of ξ_j is linked to the sign of c_j , which can—in many cases—not be tuned. For example, c_j is positive for ^{23}Na and negative for ^{87}Rb .

Appendix B: Properties of Eqs. (28)-(31)

Equations (28)-(31) imply the following:

1. The parameter ξ_1 and ξ_3 are real and their sign is determined by the sign of the coupling strengths c_1 and c_3 , respectively.
2. The parameters χ_1 and χ_3 are either purely real or purely imaginary.
 - For $-(2\bar{N}_0-1)^{-1} < q_j/q_{c,j} < (4\bar{N}_0-1)(2\bar{N}_0-1)^{-1}$ (this corresponds to $0 \lesssim q_j/q_{c,j} \lesssim 2$), χ_j is purely real.

- For $q_j/q_{c,j} \leq -(2\bar{N}_0 - 1)^{-1}$ and $q_j/q_{c,j} \geq (4\bar{N}_0 - 1)(2\bar{N}_0 - 1)^{-1}$ (this corresponds to $q_j/q_{c,j} \lesssim 0$ and $q_j/q_{c,j} \gtrsim 2$), χ_j is purely imaginary, with the imaginary part being greater than zero. In this case, it is convenient to replace χ_j by $i|\chi_j|$. Correspondingly, it is convenient to replace $\cosh(\xi_j \chi_j)$ in the expressions for A_j and B_j by $\cos(\xi_j |\chi_j|)$ and to replace $i \sinh(\xi_j \chi_j)/\chi_j$ by $i \sin(\xi_j |\chi_j|)/|\chi_j|$.

3. It follows that A_1 and A_3 are, in general, complex.

4. From points 1. and 2., it also follows that B_1 and B_3 are purely imaginary, implying that the phases γ_{B_j} are equal to $\pi/2$ when the imaginary part of B_j is positive and $-\pi/2$ when the imaginary part is negative.

Appendix C: Coherent spin state

This appendix derives the expression for the coherent spin state, Eq. (57), used in Sec. IV B within the undepleted pump approximation. The derivation starts with the coherent three-mode spin state $|\alpha_{+1}, \alpha_0, \alpha_{-1}\rangle$,

$$|\alpha_{+1}, \alpha_0, \alpha_{-1}\rangle = \underbrace{\sum_{n_{+1}=0}^N \sum_{n_0=0}^N \sum_{n_{-1}=0}^N}_{n_{+1}+n_0+n_{-1}=N} \sqrt{\frac{N!}{n_{+1}!n_0!n_{-1}!}} (\alpha_{+1})^{n_{+1}} (\alpha_0)^{n_0} (\alpha_{-1})^{n_{-1}} |n_{+1}, n_0, n_{-1}\rangle, \quad (\text{C1})$$

where the sums over the occupation numbers n_{+1} , n_0 and n_{-1} are restricted such that the number N of particles is fixed. In Eq. (C1), we have $\alpha_m = (\bar{N}_m/N)^{1/2} \exp(i\bar{\vartheta}_m)$ and $\sum_{m=+1,0,-1} |\alpha_m|^2 = 1$. This coherent three-mode spin state yields, when employed as an initial state for the time propagation under the full spin Hamiltonian \hat{H}_{spin} , results that agree up to order $1/N$ with the UPA results presented in Secs. IV B 1 and IV B 2. For example, this state is used to obtain the circles in Fig. 6(b). When using Eq. (C1), we define $\bar{\theta} = -(\bar{\vartheta}_{+1} + \bar{\vartheta}_{-1})$, i.e., we set $\bar{\vartheta}_0$ to zero. This does not pose any restrictions on our formulation since the results are independent of the overall phase factor of the initial state.

The coherent three-mode spin state can alternatively be written as

$$|\alpha_{+1}, \alpha_0, \alpha_{-1}\rangle = \frac{1}{\sqrt{N!}} \left(\alpha_{+1} \hat{a}_{+1}^\dagger + \alpha_0 \hat{a}_0^\dagger + \alpha_{-1} \hat{a}_{-1}^\dagger \right)^N |\text{vac}\rangle, \quad (\text{C2})$$

where $|\text{vac}\rangle$ denotes the vacuum state. This is the “true” vacuum state that contains no particles. It is distinct from the unseeded Fock state $|0, N, 0\rangle$, which is referred to as vacuum state throughout this paper in analogy with the photonic system. Adding $(N - \bar{N}_{+1} - \bar{N}_0 - \bar{N}_{-1}) \exp(i\bar{\vartheta}_0)$, which is equal to zero, to the terms in the round brackets in Eq. (C2), we find

$$|\alpha_{+1}, \alpha_0, \alpha_{-1}\rangle = \frac{N^{N/2} \exp(iN\bar{\vartheta}_0)}{\sqrt{N!}} \times \left[1 + \frac{\sqrt{\bar{N}_{+1}} \exp(i\bar{\vartheta}_{+1}) \hat{a}_{+1}^\dagger + \sqrt{\bar{N}_{-1}} \exp(i\bar{\vartheta}_{-1}) \hat{a}_{-1}^\dagger - \bar{N}_{+1} - \bar{N}_{-1} + \left(\sqrt{\bar{N}_0} \hat{a}_0^\dagger - \bar{N}_0 \right)}{N} \right]^N |\text{vac}\rangle, \quad (\text{C3})$$

where we defined $\bar{\theta}_{+1} = \bar{\vartheta}_{+1} - \bar{\vartheta}_0$ and $\bar{\theta}_{-1} = \bar{\vartheta}_{-1} - \bar{\vartheta}_0$. Considering the large N limit and using the identity

$$\lim_{N \rightarrow \infty} \left(1 + \frac{A}{N} \right)^N = \exp(A), \quad (\text{C4})$$

we find

$$|\alpha_{+1}, \alpha_0, \alpha_{-1}\rangle \xrightarrow{N \rightarrow \infty} \frac{N^{N/2} \exp(iN\bar{\vartheta}_0)}{\sqrt{N!}} \times \exp(-\bar{N}_{+1} - \bar{N}_{-1}) \exp\left(\sqrt{\bar{N}_{+1}} \exp(i\bar{\theta}_{+1}) \hat{a}_{+1}^\dagger + \sqrt{\bar{N}_{-1}} \exp(i\bar{\theta}_{-1}) \hat{a}_{-1}^\dagger \right) \exp\left(\sqrt{\bar{N}_0} \hat{a}_0^\dagger - \bar{N}_0 \right) |\text{vac}\rangle. \quad (\text{C5})$$

Importantly, the right hand side of Eq. (C1) is, in the large N limit, identical to Eq. (C5), i.e., Eq. (C5) is the coherent three-mode spin state for large N .

In the spirit of the undepleted pump approximation, we now replace the operator \hat{a}_0^\dagger in Eq. (C5) by $(\bar{N}_0)^{1/2}$. This replacement has the following consequences: (i) The term $\exp(\sqrt{\bar{N}_0}\hat{a}_0^\dagger - \bar{N}_0)$ goes to 1. (ii) No atoms are created in the $m = 0$ hyperfine state, i.e., the $m = 0$ mode of the three-mode state is effectively being eliminated. (iii) Expanding out the exponential that contains the operators \hat{a}_{+1}^\dagger and \hat{a}_{-1}^\dagger , it can be seen that the state is a superposition of Fock states containing varying number of atoms; this observation is closely related to point (ii) and also implies that N should now be interpreted as a parameter as opposed to the actual atom number. (iv) The state is no longer normalized to 1. Restoring the normalization and using $\beta_m = (\bar{N}_m)^{1/2} \exp(i\bar{\theta}_m)$ (see Sec. IV B), the right hand side of Eq. (C5) becomes

$$\exp(iN\bar{\vartheta}_0) \exp\left(-\frac{|\beta_{+1}|^2 + |\beta_{-1}|^2}{2}\right) \exp\left(\beta_{+1}\hat{a}_{+1}^\dagger + \beta_{-1}\hat{a}_{-1}^\dagger\right) |\text{vac}\rangle. \quad (\text{C6})$$

Except for the overall phase $\exp(iN\bar{\vartheta}_0)$, which does not have an effect on any of the observables, this is the coherent spin state, Eq. (57), used in our undepleted pump approximation calculations in Sec. IV B. We emphasize that even though the $m = 0$ mode has been effectively

eliminated from the formulation, this mode still serves as a phase reference. This can be seen from the fact that $\bar{\theta}_{+1}$ and $\bar{\theta}_{-1}$ are defined in terms of $\bar{\vartheta}_{+1}$ and $\bar{\vartheta}_{-1}$, measured relative to $\bar{\vartheta}_0$.

-
- [1] L. Pezzè, A. Smerzi, M. K. Oberthaler, R. Schmied, and P. Treutlein, “Quantum metrology with nonclassical states of atomic ensembles,” *Rev. Mod. Phys.* **90**, 035005 (2018).
- [2] D. Braun, G. Adesso, F. Benatti, R. Floreanini, U. Marzolino, M. W. Mitchell, and S. Pirandola, “Quantum-enhanced measurements without entanglement,” *Rev. Mod. Phys.* **90**, 035006 (2018).
- [3] C. M. Caves, K. S. Thorne, R. W. P. Drever, V. D. Sandberg, and M. Zimmermann, “On the measurement of a weak classical force coupled to a quantum-mechanical oscillator. I. Issues of principle,” *Rev. Mod. Phys.* **52**, 341–392 (1980).
- [4] C. M. Caves, “Quantum-mechanical noise in an interferometer,” *Phys. Rev. D* **23**, 1693–1708 (1981).
- [5] M. Pitkin, S. Reid, S. Rowan, and J. Hough, “Gravitational Wave Detection by Interferometry (Ground and Space),” *Living Reviews in Relativity* **14**, 5 (2011).
- [6] C. L. Degen, F. Reinhard, and P. Cappellaro, “Quantum sensing,” *Rev. Mod. Phys.* **89**, 035002 (2017).
- [7] W. Wasilewski, K. Jensen, H. Krauter, J. J. Renema, M. V. Balabas, and E. S. Polzik, “Quantum Noise Limited and Entanglement-Assisted Magnetometry,” *Phys. Rev. Lett.* **104**, 133601 (2010).
- [8] J. B. Brask, R. Chaves, and J. Kołodyński, “Improved Quantum Magnetometry beyond the Standard Quantum Limit,” *Phys. Rev. X* **5**, 031010 (2015).
- [9] C. Freier, M. Hauth, V. Schkolnik, B. Leykauf, M. Schilling, H. Wziontek, H.-G. Scherneck, J. Müller, and A. Peters, “Mobile quantum gravity sensor with unprecedented stability,” *Journal of Physics: Conference Series* **723**, 012050 (2016).
- [10] H. Fan, S. Kumar, J. Sedlacek, H. Kübler, S. Karimkashi, and J. P. Shaffer, “Atom based RF electric field sensing,” *J. Phys. B* **48**, 202001 (2015).
- [11] J. P. Dowling and K. P. Seshadreesan, “Quantum Optical Technologies for Metrology, Sensing, and Imaging,” *Journal of Lightwave Technology* **33**, 2359–2370 (2015).
- [12] E. Thiebaut and J. Giovannelli, “Image reconstruction in optical interferometry,” *IEEE Signal Processing Magazine* **27**, 97–109 (2010).
- [13] G. Brida, M. Genovese, and I. R. Berchera, “Experimental realization of sub-shot-noise quantum imaging,” *Nat. Photonics* **4**, 227 (2010).
- [14] B. Yurke, S. L. McCall, and J. R. Klauder, “SU(2) and SU(1,1) interferometers,” *Phys. Rev. A* **33**, 4033–4054 (1986).
- [15] M. Xiao, L.-A. Wu, and H. J. Kimble, “Precision measurement beyond the shot-noise limit,” *Phys. Rev. Lett.* **59**, 278–281 (1987).
- [16] M. J. Holland and K. Burnett, “Interferometric detection of optical phase shifts at the Heisenberg limit,” *Phys. Rev. Lett.* **71**, 1355–1358 (1993).
- [17] S. L. Braunstein and C. M. Caves, “Statistical distance and the geometry of quantum states,” *Phys. Rev. Lett.* **72**, 3439–3443 (1994).
- [18] L. Pezzè and A. Smerzi, “Entanglement, Non-linear Dynamics, and the Heisenberg Limit,” *Phys. Rev. Lett.* **102**, 100401 (2009).
- [19] S. Boixo, A. Datta, M. J. Davis, A. Shaji, A. B. Tacla, and C. M. Caves, “Quantum-limited metrology and Bose-Einstein condensates,” *Phys. Rev. A* **80**, 032103 (2009).
- [20] Y. Kawaguchi and M. Ueda, “Spinor Bose-Einstein condensates,” *Physics Reports* **520**, 253 – 381 (2012).
- [21] D. M. Stamper-Kurn and M. Ueda, “Spinor Bose gases: Symmetries, magnetism, and quantum dynamics,” *Rev. Mod. Phys.* **85**, 1191–1244 (2013).
- [22] S. Yi, Ö. E. Müstecaplıoğlu, C. P. Sun, and L. You, “Single-mode approximation in a spinor-1 atomic condensate,” *Phys. Rev. A* **66**, 011601 (2002).
- [23] M. Gabbriellini, L. Pezzè, and A. Smerzi, “Spin-Mixing Interferometry with Bose-Einstein Condensates,” *Phys. Rev. Lett.* **115**, 163002 (2015).
- [24] D. Linnemann, H. Strobel, W. Muessel, J. Schulz, R. J. Lewis-Swan, K. V. Kheruntsyan, and M. K. Oberthaler, “Quantum-Enhanced Sensing

- Based on Time Reversal of Nonlinear Dynamics,” *Phys. Rev. Lett.* **117**, 013001 (2016).
- [25] C. K. Law, H. Pu, and N. P. Bigelow, “Quantum Spins Mixing in Spinor Bose-Einstein Condensates,” *Phys. Rev. Lett.* **81**, 5257–5261 (1998).
- [26] F. Gerbier, A. Widera, S. Fölling, O. Mandel, and I. Bloch, “Resonant control of spin dynamics in ultracold quantum gases by microwave dressing,” *Phys. Rev. A* **73**, 041602 (2006).
- [27] L. Zhao, J. Jiang, T. Tang, M. Webb, and Y. Liu, “Dynamics in spinor condensates tuned by a microwave dressing field,” *Phys. Rev. A* **89**, 023608 (2014).
- [28] C. Chin, R. Grimm, P. Julienne, and E. Tiesinga, “Feshbach resonances in ultracold gases,” *Rev. Mod. Phys.* **82**, 1225–1286 (2010).
- [29] S. Choi and B. Sundaram, “Bose-Einstein condensate as a nonlinear Ramsey interferometer operating beyond the Heisenberg limit,” *Phys. Rev. A* **77**, 053613 (2008).
- [30] M. Napolitano, M. Koschorreck, B. Dubost, N. Behbood, R. J. Sewell, and M. W. Mitchell, “Interaction-based quantum metrology showing scaling beyond the Heisenberg limit,” *Nature* **471**, 486 (2011).
- [31] P. M. Anisimov, G. M. Raterman, A. Chiruvelli, W. N. Plick, S. D. Huver, H. Lee, and J. P. Dowling, “Quantum Metrology with Two-Mode Squeezed Vacuum: Parity Detection Beats the Heisenberg Limit,” *Phys. Rev. Lett.* **104**, 103602 (2010).
- [32] D. V. Tsarev, S. M. Arakelian, Y.-L. Chuang, R.-K. Lee, and A. P. Alodjants, “Quantum metrology beyond heisenberg limit with entangled matter wave solitons,” *Opt. Express* **26**, 19583–19595 (2018).
- [33] S. S. Szigeti, R. J. Lewis-Swan, and S. A. Haine, “Pumped-Up SU(1,1) Interferometry,” *Phys. Rev. Lett.* **118**, 150401 (2017).
- [34] C. D. Hamley, C. S. Gerving, T. M. Hoang, E. M. Bookjans, and M. S. Chapman, “Spin-nematic squeezed vacuum in a quantum gas,” *Nature Physics* **8**, 305 (2012).
- [35] J. P. Wrubel, A. Schwettmann, D. P. Fahey, Z. Glassman, H. K. Pechkis, P. F. Griffin, R. Barnett, E. Tiesinga, and P. D. Lett, “Spinor Bose-Einstein-condensate phase-sensitive amplifier for SU(1,1) interferometry,” *Phys. Rev. A* **98**, 023620 (2018).
- [36] M. O. Scully and M. S. Zubairy, *Quantum optics* (Cambridge University Press, 1997).
- [37] S. Knoop, T. Schuster, R. Scelle, A. Trautmann, J. Appmeier, M. K. Oberthaler, E. Tiesinga, and E. Tiemann, “Feshbach spectroscopy and analysis of the interaction potentials of ultracold sodium,” *Phys. Rev. A* **83**, 042704, (2011).

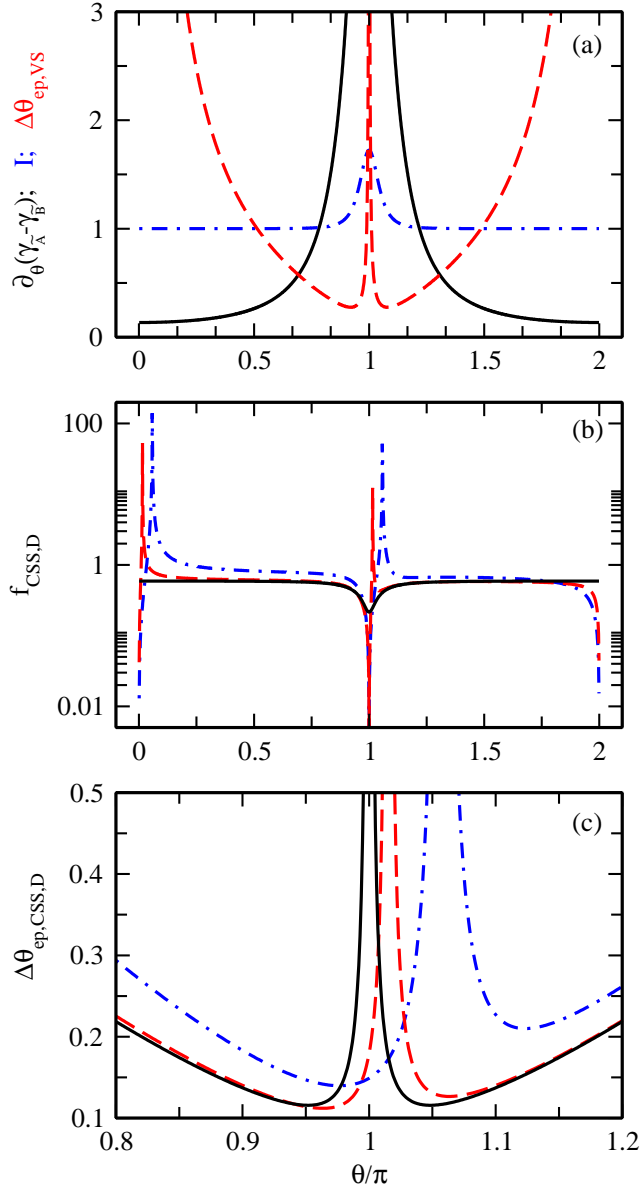


FIG. 7. (Color online) Analysis of error propagation based phase sensitivity for the resonant asymmetric interferometer with $\chi_1 = \chi_3 = \xi_1 = 1$ and $\xi_3 = 3/2$ for an initial coherent spin state with $\bar{N}_s = 2$. (a) The dashed, dash-dotted, and solid lines show $\Delta\theta_{\text{ep,VS}}$, \mathcal{I} , and $\partial_\theta(\gamma_B - \gamma_A)$, respectively, as a function of θ . (b) The solid, dashed, and dash-dotted lines show the quantity $f_{\text{CSS,D}}$ for $\bar{\theta} = \pi/2$, $\bar{\theta} = 0.36\pi$, and $\bar{\theta} = 0$, respectively, as a function of θ for a balanced initial state with $\bar{N}_+ = \bar{N}_- = 1$. Note the logarithmic scale of the vertical axis. (c) The solid, dashed, and dash-dotted lines show the phase sensitivity $\Delta\theta_{\text{ep,CSS,D}}$ for $\bar{\theta} = \pi/2$, $\bar{\theta} = 0.36\pi$, and $\bar{\theta} = 0$, respectively, as a function of θ for a balanced initial state with $\bar{N}_+ = \bar{N}_- = 1$.

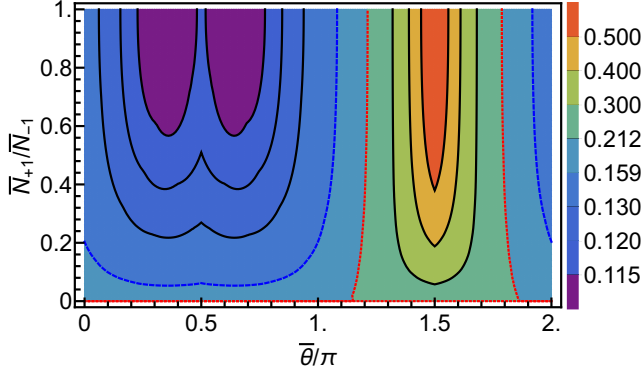


FIG. 8. (Color online) Minimum $\min(\Delta\theta_{\text{ep,CSS,D}})$ of the error propagation based phase sensitivity for the resonant asymmetric interferometer with $\chi_1 = \chi_3 = \xi_1 = 1$ and $\xi_3 = 3/2$ for an initial coherent spin state with $\bar{N}_s = 2$ as functions of \bar{N}_+/\bar{N}_- and $\bar{\theta}$. The legend on the right defines the color scheme of the contours. The contours shown in blue and red have the values 0.1592 and 0.2120, respectively. The former is equal to $\min(\Delta\theta_{\text{ep,PFS,S}})$ and the latter to $\min(\Delta\theta_{\text{ep,PFS,D}})$.

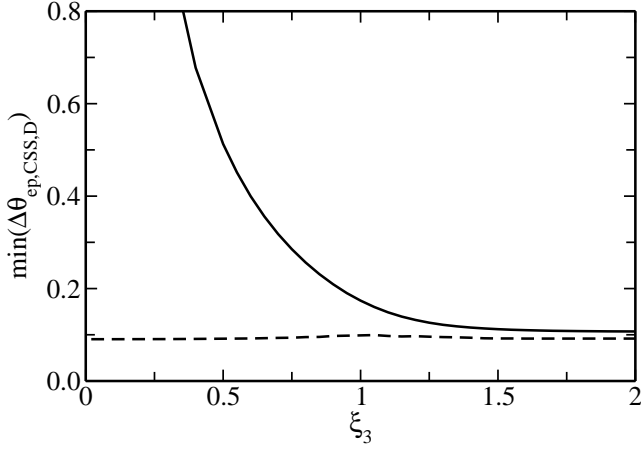


FIG. 9. Interferometer performance for the resonant interferometer with $\chi_1 = \chi_3 = \xi_1 = 1$ for a coherent spin state with double-sided seeding ($\bar{N}_s = 2$). The solid line shows the minimum $\min(\Delta\theta_{\text{ep,CSS,D}})$ of the error propagation based phase sensitivity as a function of ξ_3 ; note, the minimization is done by varying θ , $\bar{\theta}$, and \bar{N}_+/\bar{N}_- . For comparison, the dashed line shows the quantum Cramer-Rao bound $\Delta\theta_{\text{QCR}}$ for the initial states at which $\Delta\theta_{\text{ep,CSS,D}}$ takes its minimum.